frontiers in Applied Mathematics and Statistics

TYPE Original Research
PUBLISHED 06 November 2026
DOI 10.3389/fams.2026.2018430

Check for updates

Predictive modelling of conducting Casson nanofluid flow using a physics-informed neural network: effects of thermal stratification and coupled transport mechanisms

Priya Mathur[1], Amit Kumar Gupta[2]*, S. R. Mishra[3] and Hari Mohan Singh[4]

[1]Department of Mathematics, Poornima Institute of Engineering and Technology, Jaipur, India, [2]Department of Computer Science and Engineering, Manipal University Jaipur, Jaipur, India, [3]Department of Mathematics, Siksha O Anusandhan, Bhubaneswar, India, [4]Department of Information Technology, Swami Keshvanand Institute of Technology Management and Gramothan, Jaipur, India

OPEN ACCESS

EDITED BY
Vikas Chaurasiya,
National Forensic Sciences University, India

REVIEWED BY
Mohammad Jalili,
Henan Polytechnic University, China
Qusain Haider,
International School for Advanced Studies (SISSA), Italy

*CORRESPONDENCE
Amit Kumar Gupta
amit.gupta@jaipur.manipal.edu

RECEIVED 04 October 2026
REVISED 18 October 2026
ACCEPTED 18 October 2026
PUBLISHED 06 November 2026

CITATION
Mathur P, Gupta AK, Mishra SR and Singh HM (2026) Predictive modelling of conducting Casson nanofluid flow using a physics-informed neural network: effects of thermal stratification and coupled transport mechanisms. *Front. Appl. Math. Stat.* 12:2018430. doi: 10.3389/fams.2026.2018430

COPYRIGHT
© 2026 Mathur, Gupta, Mishra and Singh. This is an open-access article distributed under the terms of the Creative Commons Attribution License (CC BY). The use, distribution or reproduction in other forums is permitted, provided the original author(s) and the copyright owner(s) are credited and that the original publication in this journal is cited, in accordance with accepted academic practice. No use, distribution or reproduction is permitted which does not comply with these terms.

Conducting Casson nanofluid flow with thermal stratification plays vital role in advanced heat and mass transfer processes such as energy conversion, polymer processing, metallurgical operations, and biomedical applications. The simultaneous influence of magnetic fields, porous-medium resistance, Joule and Darcy dissipation, thermal radiation, Brownian motion, thermophoresis, and chemical reactions creates a strongly coupled nonlinear boundary-value problem that is difficult to solve using conventional analytical or numerical methods. To address this challenge, present study examines flow, heat-transfer, and mass-transfer behaviour of conducting Casson nanofluid over exponentially expanding permeable surface, incorporating thermal stratification along with aforementioned physical effects. Governing equations are reduced to a system of nonlinear ordinary differential equations through similarity transformations. Physics-Informed Neural Network framework is developed to obtain predictive solutions by embedding the governing equations, boundary conditions and loss function. PINN utilizes automatic differentiation and a two-stage training strategy with Adam and L-BFGS optimizers. The numerical performance of the PINN is assessed using governing-equation residual metrics, including MSE, MAE, and RMSE. The MSE ranges from 4.74×10^{-7} to 5.55×10^{-3}, the MAE from 4.75×10^{-4} to 5.32×10^{-2}, and the RMSE from 6.89×10^{-4} to 7.45×10^{-2} across the reported parameter cases. These metrics quantify residual satisfaction of the governing equations rather than errors relative to an external reference solution. Agreement with an independently computed boundary-value solution is assessed separately through comparisons of the solution profiles and wall quantities for selected parameter cases. Overall, the results demonstrate the applicability of the PINN framework to the coupled nonlinear conducting Casson nanofluid problem. Independent comparison with a boundary-value solution was conducted for the baseline case and the parameter variations $R_d = 1.5$ and $S_c = 0.6$. The agreement in the wall quantities for these selected cases supports the numerical consistency of the PINN predictions under the conditions examined. These findings are limited to the evaluated cases and do not establish convergence or low solution error across the entire parameter range.

KEYWORDS
Casson nanofluid, chemical reaction, Darcy dissipation, permeable medium, physics-informed neural network, thermal stratification

1 Introduction

Casson nanofluids are a class of non-Newtonian fluids that exhibit yield-stress-dependent flow behaviour and have attracted considerable attention because of their enhanced thermal and mass-transfer characteristics. Their ability to modify momentum and heat-transfer behaviour makes them relevant to a variety of engineering and industrial applications, including thermal management, energy conversion, polymer processing, metallurgical operations, and biomedical transport processes. In particular, the simultaneous consideration of magnetic fields, porous-medium effects, thermal radiation, viscous and Joule dissipation, and nanoparticle transport is important for developing realistic models of advanced heat and mass-transfer systems.

Several investigations have examined the transport characteristics of Casson and other non-Newtonian nanofluids under different physical conditions. Sankari et al. (1) investigated the double-stratified flow of a Casson nanofluid over an exponentially stretching sheet and demonstrated the importance of stratification in determining the thermal and concentration characteristics of the flow. Kumar et al. (2) examined MHD Casson nanofluid flow with activation energy, Hall current, and thermal radiation, highlighting the sensitivity of the flow and thermal fields to electromagnetic and radiative effects. Swain et al. (3) investigated viscous dissipation and Joule heating in MHD flow over a stretching surface embedded in a porous medium, emphasizing the role of energy-dissipation mechanisms in heat-transfer processes. Reddy and Maddileti (4) studied Casson nanofluid flow in the presence of Joule heating and thermal radiation and reported significant modifications in the temperature distribution. Further investigations have considered the effects of spinning surfaces, porous media, activation energy, chemical reactions, and related transport mechanisms in Casson and non-Newtonian fluids (5–9).

Recent studies (10–15) have further demonstrated that double stratification, yield stress, viscous dissipation, electromagnetic effects, slip conditions, and chemical reactions can substantially alter the momentum, thermal, and concentration fields of non-Newtonian fluids. In addition, investigations of MHD nanofluids (16–20) have considered the influence of viscous dissipation, variable thermal conductivity, chemical reactions, and different surface geometries on coupled heat and mass transfer. These studies have established that the simultaneous interaction of multiple physical mechanisms can produce highly nonlinear and strongly coupled transport behaviour. Consequently, accurate treatment of such systems is important for understanding and controlling heat and mass transfer in practical engineering configurations.

In parallel with these developments, Physics-Informed Neural Networks (PINNs) have emerged as an effective computational framework for solving nonlinear differential equations by incorporating the governing physical laws directly into the training process. Unlike conventional supervised machine-learning methods, PINNs do not necessarily require labelled datasets and can construct approximate solutions by minimizing the residuals of governing differential equations together with the prescribed boundary conditions. Reviews by Cuomo et al. (21) and Shukla et al. (22) established the potential of PINNs for solving a broad range of differential-equation-based scientific problems. Menga et al. (23) introduced Parareal PINNs for time-dependent problems, while Gin et al. (24) investigated improved training strategies for stiff systems. Regularized PINN formulations and gradient-flow improvements have also been reported by Yamazaki et al. (25) and Wang et al. (26), respectively. Furthermore, Goswami et al. (27) extended physics-informed learning toward neural operators capable of learning solution operators for parametric differential equations. These developments demonstrate the increasing potential of physics-informed learning for nonlinear and Multiphysics computational problems.

Neural-network approaches have also been applied directly to heat-transfer and nanofluid problems. Galal et al. (28) investigated heat and mass transfer between rotating permeable disks, while Hassan et al. (29) combined artificial neural networks with the BVP-4C technique to examine mixed convection in a rotating nanofluid system. Haider et al. (30) studied electrically conducting nanofluid flow under thermal radiation, slip, and heat-generation effects. Their work is relevant to the present investigation because electromagnetic and thermal mechanisms also influence the energy transport considered here. However, the present model additionally incorporates Casson rheology, thermal stratification, porous-medium resistance, Joule and Darcy dissipation, Brownian motion, thermophoresis, and chemical reactions within a unified boundary-value formulation.

Other studies have considered the mathematical and numerical treatment of non-Newtonian fluids under magnetic and porous-medium effects. Haider et al. (31) investigated heat and mass transfer in nanomaterial-based flow over a rotating cone, whereas Haider et al. (32) examined magneto-hydraulic Casson fluid flow over a porous stretching surface under suction and blowing conditions. These investigations provide useful background for the selection of governing equations, boundary conditions, and engineering quantities. Nevertheless, the differences in geometry, constitutive assumptions, and combinations of transport mechanisms mean that their results cannot be transferred directly to the present exponentially expanding surface configuration.

Recent developments have further extended neural-network methods to coupled transport and multiphysics modelling. Chari et al. (33) examined Joule heating and chemical reactions in MHD nanofluid flow. Ganji et al. (34) developed a data-driven approach for predicting thermo-solutal transport in a Casson-based radiative MHD ternary nanofluid, while Jalili et al. (35) investigated data-driven prediction of flow and thermal fields in magnetized Boger–micropolar tri-hybrid nanofluids. In addition, Ganji et al. (36) combined a physics-informed neural network with semi-analytical modelling for MHD channel flow in a porous medium. In a different application, Ganji et al. (37) proposed a physics-informed deep operator network for dynamic simulation of photovoltaic/thermal collectors. These studies illustrate the application of physics-informed learning to different transport problems, but their geometries, governing equations, and computational objectives differ from those of the present conducting Casson nanofluid model. These studies demonstrate the growing use of neural networks and physics-informed methods in

nonlinear transport problems. However, the learning strategy and physical model differ across these investigations, and their reported performance should be interpreted in the context of the corresponding governing equations and validation procedures.

Related work has also examined neural-network prediction of blood nanofluid flow in stenotic arteries (38) and the use of physics-informed deep operator learning for coupled heat and mass transport in rotating-disk systems (39). These contributions are relevant to the broader development of computational learning methods for transport phenomena. However, a supervised neural network trained on numerical reference data, a conventional PINN constrained by differential-equation residuals, and an operator-learning framework are methodologically distinct. The present work adopts a PINN to approximate the coupled similarity functions while enforcing the transformed momentum, energy, and concentration equations and their boundary conditions. The resulting solution is assessed using residual-based diagnostics and comparisons with an independently computed boundary-value solution.

Taken together, these studies provide a useful foundation for neural-network-assisted modelling and nonlinear transport analysis. Nevertheless, the simultaneous treatment of Casson rheology, magnetic and porous-medium resistance, thermal stratification, viscous and Joule heating, Darcy dissipation, Brownian motion, thermophoresis, and chemical reaction over an exponentially expanding permeable surface remains the focus of the present investigation. The principal objective is therefore not simply to apply a neural network to a fluid-flow problem, but to evaluate a physics-informed framework for this specific coupled mathematical model and to assess its predictions against an independent numerical reference for selected parameter configurations.

Despite these advances, an important research gap remains in the predictive modelling of strongly coupled Casson nanofluid systems. Existing studies have predominantly relied on analytical or conventional numerical approaches, including methods such as the Homotopy Analysis Method (HAM) and numerical shooting techniques. Such approaches may become computationally demanding or encounter convergence difficulties when several nonlinear mechanisms, including magnetic resistance, porous-medium effects, dissipative heating, nanoparticle transport, thermal stratification, and chemical reactions, act simultaneously. Moreover, the combined influence of magnetic and porous-medium effects, dissipative heating, nanoparticle transport, thermal stratification, and chemical reaction in a conducting Casson nanofluid over an exponentially expanding permeable surface has not been sufficiently investigated using a PINN-based predictive framework. The present study therefore addresses this gap by integrating the governing Multiphysics model with a physics-informed neural-network methodology and systematically examining the resulting flow, thermal, and concentration responses.

The primary objective of this investigation is to develop and evaluate a physics-informed predictive framework for the coupled flow, heat-transfer, and mass-transfer behaviour of a conducting Casson nanofluid over an exponentially expanding permeable surface. Specifically, the study aims to:

1 Formulate a mathematical model for conducting Casson nanofluid flow over an exponentially expanding permeable surface incorporating thermal stratification, magnetic effects, porous-medium resistance, dissipative heating, and nanoparticle transport mechanisms.
2 Investigate the combined influence of magnetic and porous-medium effects, including the associated Joule and Darcy dissipation mechanisms, on the momentum and thermal transport characteristics.
3 Examine nanoparticle transport mechanisms, particularly Brownian motion and thermophoresis, and their coupled influence on the temperature and concentration distributions.
4 Analyse the effects of Schmidt number, Brownian motion, and chemical reaction on the concentration field and mass-transfer behaviour.
5 Develop a Physics-Informed Neural Network (PINN) to obtain mesh-free predictive solutions of the coupled nonlinear boundary-value problem by embedding the governing equations and boundary conditions into the training loss.
6 Quantitatively evaluate the PINN predictions using the skin-friction coefficient, local Nusselt number, local Sherwood number, and statistical error measures including MSE, MAE, and RMSE.

To accomplish these objectives, the governing momentum, energy, and concentration equations are first formulated for the considered conducting Casson nanofluid configuration. Appropriate similarity transformations are then employed to convert the governing boundary-layer equations into a coupled system of nonlinear ordinary differential equations. The resulting system incorporates the effects of Casson fluid behaviour, magnetic resistance, porous-medium drag, thermal radiation, internal heat generation, Brownian motion, thermophoresis, thermal stratification, and chemical reaction.

The transformed nonlinear boundary-value problem is subsequently solved using a fully connected PINN. The neural network takes the similarity variable as its input and predicts the velocity, temperature, and concentration similarity functions. Automatic differentiation is used to evaluate the derivatives required by the governing equations, while the training loss combines the differential-equation residuals and boundary-condition errors. The computational domain is represented using 200 collocation points, and a two-stage training strategy based on the Adam and L-BFGS optimizers is employed to obtain the numerical solution.

The performance of the developed PINN is assessed through the calculated skin-friction coefficient, local Nusselt number, and local Sherwood number, which provide quantitative measures of momentum, heat, and mass transfer, respectively. In addition, MSE, MAE, and RMSE are employed to quantify the residual errors and numerical convergence of the trained PINN. The combined assessment of engineering quantities, residual-based error metrics, and physically consistent solution profiles provides a comprehensive evaluation of the numerical performance and reliability of the proposed computational framework.

The main contribution of this work is the integration of a physics-informed neural-network framework with a Multiphysics conducting Casson nanofluid model involving thermal stratification, coupled dissipative effects, magnetic and porous-medium resistance, and nanoparticle transport mechanisms. The proposed framework provides a mesh-free predictive approach for the nonlinear boundary-value problem while preserving the underlying physical constraints.

The parametric analysis is used to identify the influence of magnetic effects, porous-medium resistance, Casson behaviour, thermal radiation, Eckert number, Brownian motion, thermophoresis, thermal stratification, heat generation, Schmidt number, and chemical reaction on the flow, thermal, and concentration fields. The numerical investigation further evaluates the predictive accuracy of the PINN using engineering quantities and statistical error measures.

The remainder of the paper is organized as follows. Section 2 presents the physical configuration, governing mathematical model, similarity transformations, and boundary conditions. Section 3 describes the PINN formulation, network architecture, collocation strategy, loss-function construction, training procedure, and evaluation metrics. The numerical results and detailed parametric analysis of the velocity, temperature, and concentration profiles are presented in Section 4. The principal findings and conclusions are summarized in the final section.

2 Mathematical modelling

2.1 Physical configuration and modelling assumptions

A steady, two-dimensional, incompressible, electrically conducting Casson nanofluid flow over an exponentially expanding permeable surface is considered. The physical configuration is illustrated in Figure 1, where (x) and (y) denote the coordinates measured along and normal to the surface, respectively. The fluid occupies the region ($y > 0$), while the surface expands exponentially in the (x)-direction. The velocity of the expanding surface is prescribed as an exponentially varying function of the streamwise coordinate. The surface temperature and nanoparticle concentration are assumed to vary spatially along the expanding surface, while the corresponding free-stream temperature and concentration approach their ambient values sufficiently far from the surface. Thermal and solutal stratification are therefore incorporated into the formulation through the spatial variation of the ambient temperature and concentration fields. The Casson rheological model is employed to represent the non-Newtonian behaviour of the working fluid. An externally applied magnetic field is considered, and the fluid is assumed to be electrically conducting. The presence of a porous medium introduces Darcy resistance into the momentum transport. The interaction between the electrically conducting fluid and the applied magnetic field produces Joule heating, while viscous and porous-medium dissipation contribute to the energy transport. In addition to the momentum and thermal transport mechanisms, Brownian motion and thermophoresis are incorporated to describe nanoparticle migration. Thermal radiation and internal heat generation are also included in the energy equation. A chemical reaction term is incorporated into the concentration equation to account for the generation or consumption of the transported species. Consequently, the mathematical formulation represents a strongly coupled momentum–thermal–concentration transport system involving non-Newtonian rheology, electromagnetic effects, porous-medium resistance, dissipative heating, nanoparticle transport, thermal radiation, stratification, and chemical reaction. The mathematical formulation considered in this study follows the physical framework reported by Sankari et al. (1) for double-stratified Casson nanofluid flow over an exponentially stretching surface. In the present investigation, this formulation is used as the governing physical model and is subsequently transformed into a nonlinear boundary-value problem for solution using the proposed physics-informed neural-network (PINN) framework.

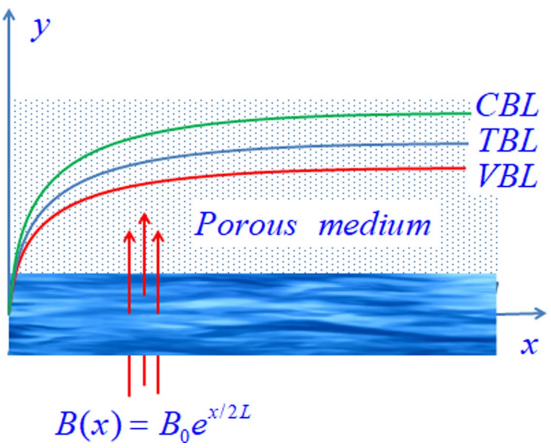


FIGURE 1
Flow configuration.

2.2 Governing equations

A Buongiorno Model nanofluid flow of conducting Casson fluid flow over an exponentially expanding permeable medium is presented in this study. The role of dissipative heat combines with both magnetic and Darcy is reported in the energy phenomenon. Moreover, the coupling effect of Brownian and thermophoresis along-side the role of higher-order reaction is vital in this investigation. The surface is expanding with a velocity $U(x) = U_0 e^{x/L}$ toward the horizontal x-direction whereas the normal direction is considered as y which is stretching with velocity $V(x) = -V_0 e^{x/L}$. The surface temperature and concentration of the proposed model considered as variable and described as $T_w(x) = T_0 + be^{x/2L}$ and $C_w(x) = C_0 + me^{x/2L}$. Here, $T_\infty(x) = T_0 + ce^{x/2L}$ and concentration $C_\infty(x) = C_0 + ne^{x/2L}$ denotes the free stream temperature and concentration, respectively, where, T_0 and C_0 are the reference temperature and concentration and b, c, m, and n are arbitrary constants. Under the above assumptions, the governing equations describing the conservation of mass, momentum, energy, and nanoparticle concentration are formulated as follows. The continuity, momentum, energy, and concentration equations are represented by Equations 1–4, respectively.

$$\frac{\partial u}{\partial x} + \frac{\partial v}{\partial y} = 0, \tag{1}$$

The continuity equation represents the conservation of mass for the incompressible flow.

$$u\frac{\partial u}{\partial x} + v\frac{\partial u}{\partial y} = \nu\left(1 + \frac{1}{\beta}\right)\frac{\partial^2 u}{\partial y^2} - \frac{\sigma B_0^2}{\rho}u - \frac{\nu}{k'}u, \tag{2}$$

The momentum equation incorporates Casson rheology, magnetic resistance, and porous-medium drag. The magnetic term

represents the Lorentz force associated with the applied magnetic field, whereas the porous-medium term accounts for the resistance to fluid motion through the permeable structure. The corresponding thermal effects are included separately in the energy equation.

$$u\frac{\partial T}{\partial x}+v\frac{\partial T}{\partial y}=\alpha\frac{\partial^2 T}{\partial y^2}+\frac{Q_0}{\rho c_p}\left(T-T_\infty\right)+\frac{16\sigma^* T_\infty^3}{3\rho c_p k^*}\frac{\partial^2 T}{\partial y^2}-\frac{\nu}{c_p}\left(1+\frac{1}{\beta}\right)\left(\frac{\partial u}{\partial y}\right)^2-\frac{\sigma B_0^2 u^2}{\rho c_p}-\tau\left[D_B\frac{\partial C}{\partial y}\frac{\partial T}{\partial y}+\frac{D_T}{T_\infty}\left(\frac{\partial T}{\partial y}\right)^2\right]+\frac{\mu}{\rho c_p K(x)}u^2 \tag{3}$$

The energy equation accounts for convective and conductive heat transport, thermal radiation, Brownian motion, thermophoresis, viscous dissipation, Joule heating, internal heat generation, and porous-medium dissipation. The viscous-dissipation contribution represents the conversion of mechanical energy into thermal energy due to fluid deformation. Joule heating arises from the interaction between the electrically conducting fluid and the applied magnetic field. The porous-medium dissipation term represents the thermal contribution associated with resistance to flow through the porous structure. Its coefficient is retained in the dimensional energy equation and must be consistent with the permeability term in the momentum equation. The corresponding dimensionless contribution is obtained by applying the similarity transformations and the parameter definitions given in Sections 2.4 and 2.7.

The momentum equation incorporates the non-Newtonian Casson rheology together with the effects of the stretching surface, applied magnetic field, and porous-medium resistance. The term $\frac{\mu}{\rho c_p K(x)}u^2$ represents the thermal energy generated by viscous resistance of the porous medium, commonly referred to as Darcy or porous-medium dissipation. The term $\frac{16\sigma^* T_\infty^3}{3\rho c_p K^*}T_{yy}$ represents thermal radiation contribution and $\frac{Q_0}{\rho c_p}\left(T-T_\infty\right)$ internal heat generation.

The energy equation accounts for convective and conductive heat transport together with the effects of thermal radiation, Brownian motion, thermophoresis, viscous/dissipative heating, Joule heating, and internal heat generation.

$$u\frac{\partial C}{\partial x}+v\frac{\partial C}{\partial y}=D_B\frac{\partial^2 C}{\partial y^2}+\frac{D_T}{T_\infty}\frac{\partial^2 T}{\partial y^2}-k_r\left(C-C_\infty\right)^2, \tag{4}$$

The concentration equation describes nanoparticle/species transport under the combined influence of convection, molecular diffusion, Brownian motion, thermophoresis, solutal stratification, and chemical reaction. The above equations are strongly coupled because the temperature and concentration fields interact through the Brownian-motion and thermophoretic mechanisms. In addition, the momentum and energy equations are coupled through the magnetic and dissipative effects. Therefore, the resulting system represents a nonlinear multiphysics boundary-layer problem.

2.3 Boundary conditions

The corresponding boundary conditions are imposed at the permeable expanding surface and in the free-stream region. At the surface, the velocity condition represents the prescribed exponential expansion together with suction or injection, while the temperature and concentration conditions represent the corresponding surface values. Far from the surface, the velocity, temperature, and concentration approach their ambient/free-stream values.

The dimensional boundary conditions are given by Equation 5.

$$\left.\begin{aligned} u&=U(x)=U_0e^{x/L},\\ v&=V(x)=-V_0e^{x/L},\\ T&=T_w(x)=T_0+be^{x/2L},\\ C&=C_w(x)=C_0+me^{x/2L} \end{aligned}\right\},\quad at\ y=0,$$
$$\left.\begin{aligned} u&\to 0, T=T_\infty(x)=T_0+ce^{x/2L},\\ C&=C_\infty(x)=C_0+ne^{x/2L} \end{aligned}\right\}\quad as\ y\to\infty. \tag{5}$$

Here, the parameter associated with the wall-normal velocity represents the suction/injection condition. Positive suction and negative blowing/injection are defined according to the convention adopted in the present formulation. These boundary conditions ensure that the velocity, temperature, and concentration fields satisfy the physical requirements at both the surface and the far-field boundary.

2.4 Similarity transformation

To reduce the governing partial differential equations to a coupled system of nonlinear ordinary differential equations, suitable similarity transformations are introduced. The transformations are selected to satisfy the continuity equation identically and to incorporate the exponential surface velocity together with the thermal and solutal stratification conditions.

The similarity transformations employed in the present investigation are given by Equation 6, where U_0 represents the reference velocity, whereas the suction velocity by $V(x)>0$ and $V(x)<0$ as suction and blowing velocity individually.

$$\left.\begin{aligned} \eta&=\sqrt{\frac{U_0}{2\nu L}}e^{x/2L}y, u=U_0e^{x/2L}f'(\eta),\\ v&=-\sqrt{\frac{\nu U_0}{2L}}e^{x/2L}\left[f(\eta)+\eta f'(\eta)\right],\\ T&=T_\infty(x)+\left(T_w(x)-T_0\right)\theta(\eta),\\ C&=C_\infty(x)+\left(C_w(x)-C_0\right)\phi(\eta) \end{aligned}\right\}. \tag{6}$$

The proposed similarity transformations satisfy the continuity equation, Equation 1, identically. Substitution of Equation 6 into the momentum, energy, and concentration equations, together with the corresponding boundary conditions, converts the original partial differential system into a coupled nonlinear ordinary differential system.

2.5 Transformed governing equations

Using the similarity transformations in Equation 6, the governing Equations 2–4 are transformed into the following dimensionless nonlinear ordinary differential equations:

$$\left(1+\frac{1}{\beta}\right)f'''+ff''-2f'^{2}-Mf'-K_{p}f'=0, \tag{7}$$

Equation 7 represents the dimensionless momentum equation and describes the combined influence of Casson non-Newtonian behaviour, magnetic resistance, porous-medium drag, and the exponential expansion of the surface.

$$\left(1+\frac{4}{3}R_{d}\right)\theta''+\Pr\begin{pmatrix}f\theta'-f'\theta-S_{t}f'+Q\theta+\\N_{b}\theta'\phi'+N_{t}\left(\theta'\right)^{2}\end{pmatrix}+$$
$$\Pr Ec\left[\left(1+\frac{1}{\beta}\right)\left(f''\right)^{2}+\left(M+K_{p}\right)\left(f'\right)^{2}\right]=0, \tag{8}$$

Equation 8 represents the dimensionless energy equation and incorporates thermal diffusion together with thermal radiation, Brownian motion, thermophoresis, dissipative heating, Joule heating, heat generation, and thermal stratification. The first term inside the bracket represents viscous/Casson dissipation, whereas $M\left(f'\right)^{2}$ and $K_{p}\left(f'\right)^{2}$ represent Joule heating and Darcy/porous-medium dissipation, respectively.

$$\phi''+Sc\left(f\phi'-f'\phi-cf'-Cr\phi^{2}\right)+\left(\frac{Nt}{Nb}\right)\theta''=0, \tag{9}$$

Equation 9 represents the dimensionless concentration equation and accounts for species diffusion, convection, Brownian motion, thermophoresis, solutal stratification, and chemical reaction. The transformed equations are mutually coupled and nonlinear. In particular, the Brownian and thermophoretic terms establish a direct interaction between the temperature and concentration fields. The presence of magnetic and porous-medium terms further influences the momentum and thermal transport. These characteristics make the resulting boundary-value problem challenging for conventional analytical and numerical techniques and provide the motivation for employing the PINN methodology developed in Section 3.

2.6 Transformed boundary conditions

The boundary conditions corresponding to the transformed system are obtained by substituting the similarity transformations into Equation 5. The resulting dimensionless boundary conditions are given by Equation 10.

$$\left.\begin{array}{l}f'(\eta)=1,\quad f(\eta)=S,\quad \theta(\eta)=1-S_{t},\\ \phi(\eta)=1-c,\quad at\ \eta=0,\\ f'(\eta)\to 0,\quad \theta(\eta)\to 0,\\ \phi(\eta)\to 0,\quad as\ \eta\to\infty\end{array}\right\}. \tag{10}$$

Here, (S) denotes the suction/injection parameter, S_{t} denotes the thermal-stratification parameter, (c) denotes the solutal-stratification parameter, and S_{c} denotes the Schmidt number. The solutal-stratification parameter c determines the wall concentration condition, $\phi(0)=1-c$, whereas the far-field concentration satisfies $\phi(\eta)\to 0$ as $\phi(\eta)\to\infty$. The Schmidt number S_{c} characterizes the relative contribution of momentum diffusivity and mass diffusivity and enters the concentration transport equation. Thus, c and S_{c} represent distinct physical quantities and must not be interchanged in the boundary conditions or numerical implementation.

where the prime denotes differentiation with respect to η, porous structure, $K_{p}=\frac{2L_{v}}{k^{*}U_{0}}$ magnetic stricture $M=\frac{2\sigma B_{0}^{2}L}{\rho U_{0}}$, Prandtl number $\Pr=\frac{\nu}{\alpha}$, heat source structure $Q=\frac{2LQ_{0}}{U_{0}\rho c_{p}}$, thermally stratified structure $T=\frac{c}{b}$, Schmidt number $Sc=\frac{\nu}{D}c=\frac{n}{m}$ chemically stratified structure $Cr=\frac{k_{0}L}{U_{0}}$, $S=\frac{V_{0}}{\sqrt{\frac{\nu U_{0}}{2L}}}S>0$ is the suction stricture, while $S<0$ is the blowing stricture. The transformed boundary conditions ensure that the predicted velocity, temperature, and concentration profiles satisfy the prescribed wall conditions and approach their physically appropriate ambient values away from the surface.

2.7 Dimensionless parameters

The transformed equations contain several dimensionless parameters that characterize the relative importance of the different physical mechanisms. The principal parameters considered in the present study include the Casson parameter, magnetic parameter, porous-medium parameter, Prandtl number, Eckert number, thermal radiation parameter, Brownian motion parameter, thermophoresis parameter, thermal stratification parameter, Schmidt number, solutal stratification parameter, chemical reaction parameter, heat-generation parameter, and suction/injection parameter. The physical interpretation of these parameters is summarized in Table 1.

The Schmidt number Sc and the solutal-stratification parameter c have distinct roles in the mathematical model. The Schmidt number represents the ratio of momentum diffusivity to mass diffusivity and appears in the dimensionless concentration transport equation. The solutal-stratification parameter describes the influence of ambient concentration stratification and determines the wall concentration condition $\phi(0)=1-c$. Although c is retained in the governing formulation, its parametric influence is not investigated in the present study. The concentration-field analysis instead focuses on the Schmidt number, Brownian motion, thermophoresis, and chemical reaction.

The exact mathematical definitions of these parameters are those appearing in the transformed Equations 7–9. In the adopted sign convention, ($S>0$) represents suction at the surface, whereas ($S<0$) represents blowing/injection.

Although the solutal stratification parameter is retained in the governing formulation to preserve the coupled mathematical model, its parametric influence is not investigated in the present study; the concentration-field analysis instead focuses on the Schmidt number, Brownian motion, thermophoresis, and chemical reaction.

TABLE 1 Physical interpretation of parameters used in the study.

Parameter	Physical significance
(β)	Casson/non-Newtonian parameter
(M)	Magnetic interaction parameter
(K)	Porous-medium/Darcy resistance parameter
(Pr)	Prandtl number
(Ec)	Eckert number
(Rd)	Thermal radiation parameter
(Nb)	Brownian motion parameter
(Nt)	Thermophoresis parameter
(St)	Thermal stratification parameter
(c)	Solutal-stratification parameter controlling the wall concentration condition
(Sc)	Schmidt number, representing the ratio of momentum diffusivity to mass diffusivity
(Kr)	Chemical reaction parameter
(Q)	Heat-generation parameter
(S)	Suction/injection parameter

2.8 Engineering quantities of interest

The engineering quantities of primary interest are the local skin-friction coefficient, local Nusselt number, and local Sherwood number. These quantities provide measures of wall shear stress, heat-transfer rate, and mass-transfer rate, respectively.

The dimensional forms of these quantities are first defined from the wall gradients of velocity, temperature, and concentration. Using the similarity transformations in Equation 6, the corresponding dimensionless forms are obtained as given in Equation 11.

The physical significance of the factors presenting local skin friction is reported as $Cf_x = \frac{\tau_w}{\frac{1}{2}\rho U^2}$, where the local Nusselt and Sherwood numbers are described as $Nu_x = \frac{xq_w}{k(T_w - T_\infty)}$, $Sh_x = \frac{xJ_w}{D(C_w - C_\infty)}$ respectively. Were

$$\tau_w = \mu\left(\frac{\partial u}{\partial y}\right)_{y=0}, q_w = -k\left(\frac{\partial T}{\partial y}\right)_{y=0}, J_w = -D\left(\frac{\partial C}{\partial y}\right)_{y=0}. \quad (11)$$

The transformation of the above expression with the help of Equation 6 are presented as by Equation 12.

$$f''(0) = Cf_x\sqrt{2/Re_x}\sqrt{\frac{x}{L}}, -\theta'(0) = \frac{Nu_x(1-S_T)}{\sqrt{2/Re_x}\sqrt{\frac{x}{L}}},$$
$$-\phi'(0) = \frac{Sh_x(1-S_C)}{\sqrt{2/Re_x}\sqrt{\frac{x}{L}}} \quad (12)$$

The local skin-friction coefficient is used to quantify the wall shear stress generated by the Casson nanofluid. The local Nusselt number characterizes the rate of heat transfer from the surface to the fluid, whereas the local Sherwood number represents the corresponding mass-transfer rate.

These quantities are subsequently evaluated from the PINN-predicted similarity functions and their derivatives. Since automatic differentiation provides smooth derivatives of the neural-network outputs, the proposed framework allows the wall-gradient-dependent engineering quantities to be evaluated directly from the learned solution.

2.9 Link between the mathematical model and the PINN framework

The mathematical formulation developed in this section produces a coupled nonlinear boundary-value problem consisting of Equations 7–9 subject to the boundary conditions in Equation 10. Rather than applying a conventional mesh-based discretization or an analytical approximation, the present study employs a physics-informed neural network to obtain predictive solutions of this transformed system.

In the PINN formulation, the similarity variable (η) is supplied to the neural network as the input, while the network predicts the dimensionless velocity, temperature, and concentration functions. Automatic differentiation is used to calculate the derivatives required in Equations 7–9. The governing-equation residuals and boundary-condition errors are then incorporated into the PINN loss function. The PINN loss function is constructed from the governing-equation residuals and boundary-condition errors. The monotonicity of the predicted temperature and concentration profiles is assessed from the resulting numerical solutions rather than being explicitly enforced through an additional loss term. The PINN therefore provides a mesh-free solution of the mathematical model without requiring labelled training data or precomputed numerical solutions. The detailed network architecture, collocation strategy, loss-function formulation, training procedure, and error-evaluation methodology are presented in Section 3.

In this manner, the mathematical model adopted from the established physical framework (1) serves as the governing physics, while the principal computational contribution of the present study is the development and application of the PINN-based predictive framework for the resulting strongly coupled nonlinear Casson nanofluid problem.

3 Solution methodology

The mathematical formulation developed in Section 2 results in a coupled nonlinear boundary-value problem consisting of

Equations 7–9, subject to the boundary conditions given in Equation 10. In the present study, this nonlinear system is solved using a Physics-Informed Neural Network (PINN). Unlike conventional mesh-based numerical methods, the proposed PINN approximates the unknown similarity functions and incorporates the governing differential equations and boundary conditions directly into the training objective. The overall computational procedure consists of five main stages: (i) generation of collocation points within the computational domain, (ii) prediction of the velocity, temperature, and concentration fields using the neural network, (iii) evaluation of the required derivatives using automatic differentiation, (iv) construction of the governing-equation and boundary-condition residuals, and (v) optimization of the network parameters using a two-stage Adam–L-BFGS strategy. The trained PINN is subsequently employed to obtain the velocity, temperature, and concentration profiles and to evaluate the associated engineering quantities.

The initial approximations used to initialize the solution fields are defined as Equation 13:

$$f_0(\eta)=1+S-e^{-\eta},\theta_0(\eta)=(1-S_t)e^{-\eta},\phi_0(\eta)=(1-c)e^{-\eta} \quad (13)$$

These initial approximations provide physically consistent starting profiles for the three dependent variables and are used to facilitate the subsequent optimization of the neural-network parameters.

The initial concentration approximation is constructed using the solutal-stratification parameter c so that it is consistent with the wall concentration condition in Equation 10. The Schmidt number S_c is retained in the concentration transport equation and is not substituted for c in the initial approximation or boundary conditions.

3.1 Physics-Informed Neural Network

The present study develops a Physics-Informed Neural Network (PINN)-based computational methodology to solve the nonlinear boundary-value problem governing magnetohydrodynamic (MHD) Casson nanofluid flow with thermal stratification and coupled nanoparticle-transport effects, viscous dissipation, and Joule heating over an exponentially stretching surface. While several existing studies have employed analytical and semi-analytical techniques such as the Homotopy Analysis Method (HAM), the present methodology employs a PINN framework in which the governing physical laws are incorporated directly into the neural-network training process. PINNs provide a mesh-free and differentiable approximation of the solution fields and allow the nonlinear differential operators to be evaluated through automatic differentiation. This characteristic makes the approach suitable for strongly coupled nonlinear systems involving momentum, thermal, and concentration transport (40–45). In the present formulation, the similarity variable (η) is supplied to the neural network as the single input, while the dimensionless velocity, temperature, and concentration functions, ($f(\eta)$, $\theta(\eta)$, and $\phi(\eta)$), respectively, are obtained as the three network outputs, as illustrated in Figure 2. Consequently, the PINN provides a unified representation of the coupled solution fields.

The transformed momentum, energy, and concentration equations incorporate the principal physical mechanisms considered in the mathematical model, including thermal stratification together with magnetic, porous-medium, thermal, and nanoparticle-transport effects. The momentum equation describes the influence of surface stretching, magnetic interaction, porous-medium resistance, and the Casson fluid characteristics on the velocity field. The energy equation accounts for convective heat transport together with Brownian motion, thermophoresis, viscous dissipation, Joule heating, thermal radiation, heat generation, and thermal stratification. Similarly, the concentration equation represents the coupled transport of nanoparticles or solute under the effects of convection, solutal stratification, Brownian diffusion, thermophoresis, and chemical reaction. The three governing equations are strongly coupled because the velocity field influences the thermal and concentration fields, while the temperature and concentration fields are mutually coupled through the thermophoretic and Brownian-motion contributions. Together with the wall and far-field boundary conditions, these equations form a nonlinear boundary-value problem that may exhibit strong gradients and stiffness for certain parameter combinations. The PINN formulation addresses this problem by minimizing the residuals of the governing equations and boundary conditions simultaneously. Thus, the physical constraints are incorporated directly into the optimization process rather than being imposed through a conventional spatial discretization (40–45).

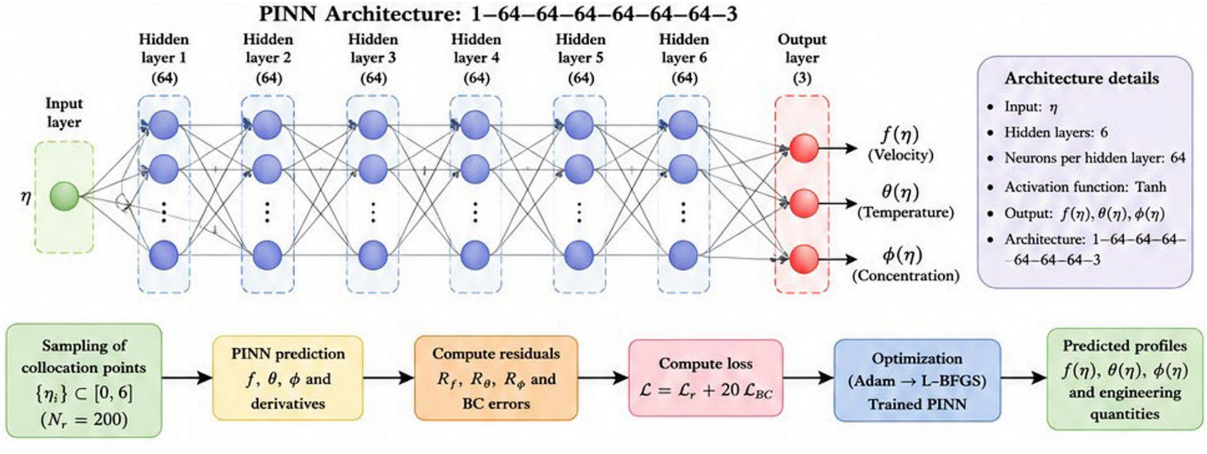


FIGURE 2
Schematic representation of the proposed Physics-Informed Neural Network architecture and training procedure.

3.2 Physics-informed neural network architecture

The proposed PINN employs a fully connected feed-forward neural network to approximate the three unknown similarity functions $f(\eta)$, $\theta(\eta)$, and $\phi(\eta)$. The network receives the scalar similarity variable (\eta) as its input and produces three outputs corresponding to the predicted velocity, temperature, and concentration fields. This compact input–output structure enables the complete coupled boundary-layer system to be represented within a single neural network. The network used in the present study consists of six fully connected hidden layers, with 64 neurons in each hidden layer. The hyperbolic tangent (Tanh) activation function is employed in the hidden layers because it is smooth and possesses continuous higher-order derivatives, which are important for evaluating the derivatives required by the governing differential equations. The selected network depth and width provide sufficient expressive capacity for representing the nonlinear solution profiles while maintaining a manageable number of trainable parameters. The architecture and the corresponding training workflow are illustrated in Figure 2.

An important advantage of the PINN formulation is that the derivatives of the network outputs can be evaluated using automatic differentiation. In the present problem, the required derivatives include f', f'', f''', θ'', and ϕ''. Automatic differentiation evaluates these derivatives directly from the computational graph of the neural network, thereby avoiding the truncation errors associated with finite-difference approximations of derivatives. The calculated derivatives are subsequently substituted into the residual forms of the momentum, energy, and concentration equations. Instead, the network parameters are optimized by minimizing a loss function constructed from the governing-equation residuals and boundary-condition residuals. This physics-informed training procedure enables the PINN to obtain continuous and differentiable approximations of the velocity, temperature, and concentration profiles.

PINN Architecture sensitivity analysis—To ensure the robustness of the proposed PINN framework, we conducted a sensitivity analysis by varying the number of hidden layers and neurons per layer. The performance was evaluated using mean squared error (MSE), mean absolute error (MAE), and convergence speed. Table 2 presents the PINN architecture sensitivity analysis, showing how variations in the number of hidden layers and neurons affect the MSE, MAE, and convergence speed.

The choice of six hidden layers with 64 neurons was based on sensitivity analysis. Smaller networks underfit, while larger ones increased training cost without significant accuracy gains. This architecture provided the best balance between accuracy and efficiency.

3.3 Collocation points

The computational domain is truncated to $0 \le \eta \le 6$. In the present implementation, 200 collocation points are generated using uniform spacing over this interval, including the two endpoints. The points are constructed using a linear spacing procedure,

$$\eta_i = \frac{i\eta_{\max}}{N_c - 1}, \qquad i = 0,1,\ldots,N_c - 1,$$

where N_c =200 and $\eta_{\max} = 6$. The governing-equation residuals are evaluated at these points using automatic differentiation. The same collocation-point generation procedure is used for the reported parameter cases. To assess the sensitivity of the solution to collocation-point density, the wall quantities and predicted profiles are compared for different values of N_c, while keeping the governing equations, boundary conditions, network architecture, loss weights, and optimization settings unchanged.

The computational domain is discretized using uniformly distributed collocation points, at which the governing-equation residuals are evaluated through automatic differentiation. To investigate the sensitivity of the physics-informed neural network (PINN) solution to collocation-point density, full-training experiments were conducted using 100, 200, 400, and 1,000 collocation points. The governing equations, boundary conditions, network architecture, loss weights, optimizer settings, and random seed were kept unchanged across the experiments.

Each configuration was trained for 3,000 Adam epochs, followed by an L-BFGS optimization stage with a maximum of 200 iterations. The velocity, temperature, and concentration profiles were evaluated on a common grid and compared with an independently computed boundary-value problem (BVP) solution. The wall quantities $f''(0), -\theta'(0)$ and $-\varphi'(0)$ were used to assess the sensitivity of the predicted wall gradients to the number of collocation points. The relative changes in the wall quantities between successive point densities were calculated. The maximum changes were approximately 0.0231% for $f''(0)$, 0.1139% for $-\theta'(0)$), and 0.0430% for $-\varphi'(0)$. The corresponding profile errors were also evaluated using the mean absolute error (MAE), root mean squared error (RMSE), and maximum absolute error relative to the BVP solution. Although the wall quantities exhibited

TABLE 2 Sensitivity analysis of PINN architecture based on network configuration, MSE, MAE, and convergence performance.

Architecture (layers × neurons)	MSE (avg)	MAE (avg)	Epochs to convergence	Remarks
3 × 32	1.2×10^{-4}	2.1×10^{-2}	1,800	Underfitting, slower convergence
4 × 64	8.7×10^{-5}	1.6×10^{-2}	1,500	Improved accuracy
6 × 64 (chosen)	4.7×10^{-5}	9.8×10^{-3}	**1,200**	Best balance of accuracy and efficiency
8 × 128	4.5×10^{-5}	9.5×10^{-3}	2,200	Marginal gain, high cost

The Bold Value indicates the number of epoch are chosen as it reflect the Best balance of accuracy and efficiency.

TABLE 3 Collocation-point sensitivity of wall quantities and relative percentage changes.

Collocation points Nc	Final total loss	Final ODE residual loss	Final boundary loss	$f''(0)$	$-\theta'(0)$	$-\phi'(0)$
100	7.58391×10^{-6}	7.54003×10^{-6}	4.38803×10^{-9}	−0.918351	0.649874	0.474161
200	7.11215×10^{-6}	7.09582×10^{-6}	1.63307×10^{-9}	−0.918339	0.649831	0.474062
400	5.46518×10^{-6}	5.36371×10^{-6}	1.014698×10^{-8}	−0.918518	0.650494	0.474149
1,000	6.59114×10^{-6}	6.56387×10^{-6}	2.72738×10^{-9}	−0.918306	0.649753	0.473945
Comparison	Change in $f''(0)$ (%)		Change in $-\theta'(0)$ (%)		Change in $-\phi'(0)$ (%)	
100 → 200	0.001311		0.006686		0.020804	
200 → 400	0.019497		0.101969		0.018338	
400 → 1,000	0.023089		0.113905		0.042967	

relatively small variations over the tested range, the profile errors did not decrease monotonically with increasing collocation-point density. The results therefore indicate limited sensitivity of the wall quantities for the baseline configuration and tested training settings; they do not establish universal convergence for all parameter combinations.

3.3.1 Sensitivity-study equations

The wall quantities to compare are

$$q_1 = f''(0), \quad q_2 = -\theta'(0), \quad q_3 = -\phi'(0).$$

Here, $f''(0)$ represents the wall velocity-gradient quantity, $-\theta'(0)$ represents the dimensionless wall heat-transfer quantity, and $-\phi'(0)$ represents the dimensionless wall mass-transfer quantity.

The percentage change between successive collocation-point counts is calculated as

$$\Delta q\,(\%) = \frac{\left|q(Nc) - q(2Nc)\right|}{\left|q(2Nc)\right|} \times 100$$

where $q(Nc)$ is the wall quantity obtained using Nc collocation points and $q(2Nc)$ is the corresponding value obtained after doubling the number of points. Table 3 shows the sensitivity of wall quantities to the number of collocation points and percentage variation in wall quantities, respectively.

The sensitivity of the PINN solution to collocation-point density is evaluated by comparing the wall quantities obtained using N_c =100, N_c =200, N_c =400 and N_c =1,000. The percentage changes in the wall velocity-gradient, heat-transfer, and mass-transfer quantities are calculated to quantify the differences between successive cases. The predicted velocity, temperature, and concentration profiles are also compared over the computational domain. Small differences in the wall quantities and profiles with increasing N_c would indicate that the numerical solution is relatively insensitive to collocation-point density over the tested range. The conclusion regarding convergence is drawn from the calculated results rather than from the number of collocation points alone.

To further examine the sensitivity of the PINN solution to the number of collocation points, the predicted velocity, temperature, and concentration profiles were compared with the corresponding independent boundary-value problem (BVP) solutions. The mean absolute error (MAE), root mean squared error (RMSE), and maximum absolute error were calculated for each profile using 100, 200, 400, and 1,000 collocation points. The results are summarized in Table 4. These measures provide a direct assessment of the differences between the PINN predictions and the independent numerical reference solution. Figure 3 compares the velocity, temperature, and concentration profiles obtained using different numbers of collocation points with the corresponding independent BVP solutions. The comparisons show the differences between the PINN predictions and the numerical reference profiles across the computational domain. The error values reported in Table 3 provide a quantitative measure of these differences. The profile errors do not decrease monotonically as the number of collocation points increases. Therefore, increasing the collocation-point density alone does not guarantee a reduction in the profile error under the present training configuration.

3.4 Loss function formulation

The PINN converts the nonlinear boundary-value problem into an optimization problem by defining a composite loss function. The total loss consists of the governing-equation residual loss and the boundary-condition loss. It is expressed as Equation 14:

$$L_{\text{total}} = \mathcal{L}_{\text{ODE}} + \lambda_{\text{BC}}\mathcal{L}_{\text{BC}} \tag{14}$$

where $\mathcal{L}_{\text{ODE}}$ represents the mean-squared residuals of the momentum, energy, and concentration equations, and $\mathcal{L}_{\text{BC}}$ represents the boundary-condition loss. The coefficient λ_{BC} controls the relative contribution of the boundary-condition loss. In the inspected implementation, this coefficient is set to 10. The optimization objective is to minimize the total loss while satisfying the governing equations and prescribed boundary conditions as closely as possible.

The ODE residual loss is defined as Equation 15:

$$\mathcal{L}_{\text{ODE}} = \text{MSE}\left(R_f\right) + \text{MSE}\left(R_\theta\right) + \text{MSE}\left(R_\phi\right) \tag{15}$$

The residuals R_f, R_θ, and R_ϕ correspond to the momentum, energy, and concentration equations, respectively. By minimizing

TABLE 4 Profile errors relative to the independent BVP solution.

Points	Profile	MAE	RMSE	Maximum absolute error
100	$f(\eta)$	0.00007353	0.00011570	0.00031640
100	$\theta(\eta)$	0.00026620	0.00036525	0.00074602
100	$\phi(\eta)$	0.00010251	0.00012502	0.00025598
200	$f(\eta)$	0.00004398	0.00006238	0.00018404
200	$\theta(\eta)$	0.00034697	0.00048595	0.00095566
200	$\phi(\eta)$	0.00003865	0.00005234	0.00014051
400	$f(\eta)$	0.00005668	0.00009401	0.00029838
400	$\theta(\eta)$	0.00021630	0.00025666	0.00046175
400	$\phi(\eta)$	0.00016672	0.00018788	0.00029454
1,000	$f(\eta)$	0.00009102	0.00014002	0.00035549
1,000	$\theta(\eta)$	0.00036531	0.00047129	0.00090313
1,000	$\phi(\eta)$	0.00013172	0.00015501	0.00028157

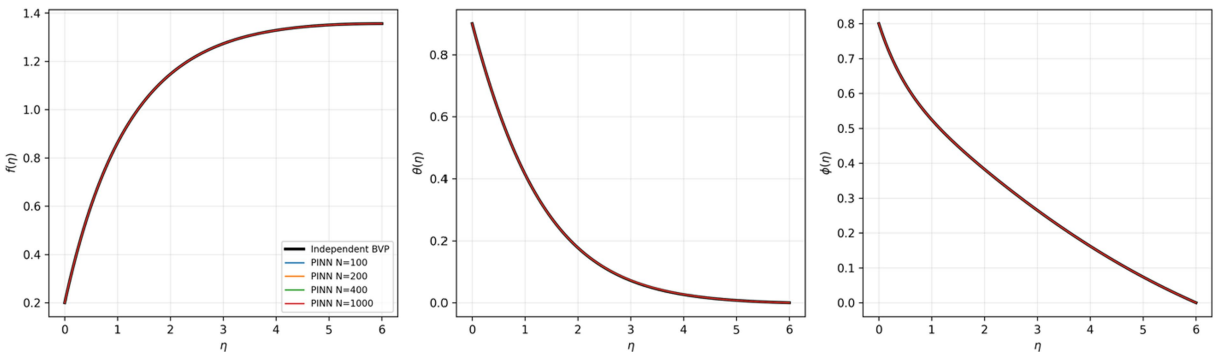


FIGURE 3
Comparison of the PINN velocity, temperature, and concentration profiles with the independent BVP solution for 100, 200, 400, and 1,000 collocation points under the same training configuration.

these residuals at the collocation points, the PINN is constrained to approximate functions that satisfy the complete nonlinear differential system.

3.5 ODE residual loss

The first major component of the total loss is the governing-equation residual loss. The residuals are obtained by substituting the neural-network predictions and their derivatives, evaluated using automatic differentiation, into Equations 7–9.

For the momentum equation, the residual is defined as Equation 16 (40–47):

$$R_f = \left(1+\frac{1}{\beta}\right) f''' + ff'' - 2\left(f'\right)^2 - \left(M + K_p\right) f' \tag{16}$$

The corresponding energy-equation residual as Equation 17:

$$R_\theta = \left(1+\frac{4}{3}R_d\right)\theta'' + \Pr\begin{pmatrix} f\theta' - f'\theta - S_t f' + Q\theta + \\ Nb\theta'\phi' + Nt\left(\theta'\right)^2 \end{pmatrix} + \Pr Ec\left[\left(1+\frac{1}{\beta}\right)\left(f''\right)^2 + \left(M+K_p\right)\left(f'\right)^2\right] = 0 \tag{17}$$

The concentration residual is expressed as Equation 18:

$$R_\phi = \phi'' + Sc\left(f\phi' - f'\phi - cf' - Cr\phi^2\right) + \left(\frac{Nt}{Nb}\right)\theta'' \tag{18}$$

The residuals are evaluated at all collocation points, and their mean-squared values constitute the ODE residual loss in Equation 15.

Minimization of these residuals forces the neural-network approximation to satisfy the nonlinear momentum, energy, and concentration equations throughout the computational domain.

3.6 Boundary condition loss

In addition to satisfying the governing equations in the interior of the computational domain, the PINN must satisfy the boundary conditions prescribed at the wall and in the far field. To enforce these requirements, a boundary-condition loss term is incorporated into the total loss function.

The boundary-condition loss is defined as Equation 19:

$$\mathcal{L}_{\mathrm{BC}} = \left|f(0)-S\right|^2 + \left|f'(0)-1\right|^2 + \left|\theta(0)-(1-St)\right|^2 + \left|\phi(0)-(1-c)\right|^2 + \left|f'(\eta_\infty)\right|^2 + \left|\theta(\eta_\infty)\right|^2 + \left|\phi(\eta_\infty)\right|^2 \quad (19)$$

For the concentration field, the wall boundary-condition residual is defined as $r_{\phi,w} = \phi_{\mathrm{PINN}}(0)-(1-c)$. where c is the solutal-stratification parameter. The far-field residual is defined as $r_{\phi,\infty} = \phi_{\mathrm{PINN}}(\eta_{\max})$, consistent with the condition $\phi(\eta)\to 0$ as $\phi(\eta)\to\infty$. The Schmidt number S_c appears in the concentration transport equation and is not substituted for c in the wall boundary-condition residual.

The first four terms enforce the wall boundary conditions, while the remaining terms enforce the far-field conditions. Specifically, the velocity gradient approaches zero in the far field, while the dimensionless temperature and concentration fields approach their ambient values. The boundary-condition loss is essential because minimizing the ODE residual alone does not guarantee that the resulting solution satisfies the prescribed boundary conditions. The combined use of the ODE residual and boundary-condition losses therefore ensures that the trained PINN satisfies both the local governing physics and the global boundary constraints (40–47).

3.7 Assessment of profile monotonicity and smoothness

The temperature and concentration profiles are examined to assess their monotonicity and smoothness over the computational domain. For non-increasing temperature and concentration profiles, the derivatives should satisfy $\theta'(\eta)\le 0$ and $\varnothing'(\eta)\le 0$, respectively. These conditions provide criteria for evaluating the predicted profiles. However, no explicit monotonicity penalty is included in the training loss used to obtain the reported results. Therefore, compliance with these conditions must be assessed directly from the computed profiles rather than assumed from the PINN formulation. The smoothness of the predicted profiles is likewise assessed from their variation across the computational domain. The Tanh activation function provides a differentiable neural-network representation, but smoothness of the activation function alone does not guarantee that the resulting solution is physically valid or monotonic. Accordingly, the predicted profiles are interpreted together with the governing-equation residuals, boundary-condition errors, and independent numerical comparison.

3.8 PINN model training

The PINN is trained using a two-stage optimization procedure consisting of the Adam optimizer followed by L-BFGS refinement. The fully connected neural network contains six hidden layers with 64 neurons per layer and uses the Tanh activation function. The Adam optimizer is configured with a learning rate of 10^{-4} and is run for 3,000 iterations. Gradient clipping is applied with a maximum gradient norm of 100 to limit excessively large parameter updates during training.

After the Adam stage, the network parameters are refined using the L-BFGS optimizer. The implementation specifies a learning rate of 1.0, a maximum of 200 iterations, a history size of 50, and strong-Wolfe line search. The stopping tolerances are set to 10^{-9} for the gradient and 10^{-12} for the loss change. The L-BFGS stage minimizes the same loss function used during Adam training.

The total loss consists of the governing-equation residual loss and the boundary-condition loss, with the latter multiplied by a fixed weight of 10. No additional monotonicity or third-derivative smoothness penalty is included in the implemented training objective. The random seed is set to 1234 for Python, NumPy, and PyTorch. Single-precision floating-point arithmetic (float32) is used, and the number of CPU threads is restricted to one. The implementation uses PyTorch, with the framework version recorded by the notebook at runtime.

The numerical performance is assessed using the governing-equation residuals, boundary-condition errors, wall quantities, and comparison with an independently computed boundary-value solution. Although the fixed random seed supports reproducibility of the initialization under the same computational environment, the present study does not include a systematic comparison of independent training runs using different random seeds. Consequently, consistency across independent initializations is not claimed and remains a subject for further investigation.

The convergence of the PINN should be assessed using the total loss, individual residual components, and the stability of the engineering quantities Cf_x , Nu_x , and Sh_x . For complete reproducibility, the final implementation should report the L-BFGS maximum iterations and stopping tolerances used in the computation. The optimization process does not require labelled training data or precomputed reference profiles. Instead, the neural-network parameters are determined by minimizing the physics-based loss function. The final trained PINN therefore represents a continuous approximation of the solution satisfying the coupled governing equations and the prescribed boundary conditions.

3.9 Evaluation of physical quantities

After completion of the training process, the PINN provides continuous and differentiable approximations of the similarity functions $f(\eta)$, $\theta(\eta)$, and $\phi(\eta)$. These functions are subsequently used to calculate the engineering quantities of practical interest, namely the skin-friction coefficient, local Nusselt number, and local Sherwood number.

The skin-friction coefficient represents the wall shear stress and is related to the wall gradient of the velocity field. In terms of the similarity solution, it is expressed proportionally as Equation 20:

$$C_f \propto -f''(0) \quad (20)$$

The corresponding sign and magnitude of C_f are interpreted according to the sign convention defined in the mathematical formulation. The dependence of the skin-friction coefficient on the magnetic parameter, porous-medium parameter, suction/blowing parameter,

and Casson parameter can therefore be investigated using the trained PINN.

The local Nusselt number characterizes the heat-transfer rate at the surface and is related to the wall temperature gradient according as Equation 21:

$$Nu_x \propto -\theta'(0) \tag{21}$$

The quantity $-\theta'(0)$ represents the nondimensional wall temperature gradient and provides a measure of the heat-transfer behaviour. It is influenced by the thermal stratification, Brownian motion, thermophoresis, thermal radiation, viscous dissipation, Joule heating, and other thermal transport mechanisms included in the governing energy equation.

Similarly, the local Sherwood number characterizes the mass-transfer rate at the surface and is related to the wall concentration gradient as Equation 22:

$$Sh_x \propto -\phi'(0) \tag{22}$$

The wall concentration gradient $\phi'(0)$ is affected by convection, solutal stratification, Brownian motion, thermophoresis, and the chemical reaction contribution. The concentration equation is also coupled with the temperature field through the thermophoretic contribution involving θ'. Consequently, an accurate prediction of Sh_x provides an additional assessment of the PINN's ability to capture the coupled heat and mass-transfer behaviour.

3.10 PINN error and convergence metrics

In addition to the engineering quantities, the numerical accuracy of the trained PINN is further evaluated using the Mean Squared Error (MSE), Root Mean Squared Error (RMSE), and Mean Absolute Error (MAE). In addition to the governing-equation residuals and boundary-condition errors, quantitative error metrics are employed to assess the numerical convergence and internal consistency of the proposed PINN solution. The Mean Squared Error (MSE), Root Mean Squared Error (RMSE), and Mean Absolute Error (MAE) are used to quantify the magnitude of the residual errors associated with the predicted solution. These metrics provide complementary measures for assessing the numerical quality and convergence behaviour of the trained PINN.

Since PINNs are trained by enforcing the governing equations and boundary conditions rather than by fitting labelled solution data, the present study evaluates the trained network primarily through physics-based residuals and convergence diagnostics. The MSE, RMSE, and MAE are calculated from the residual errors of the governing equations and are used to quantify the degree to which the neural-network solution satisfies the mathematical model. These metrics are therefore treated as internal numerical diagnostics of the PINN rather than as measures of agreement with an external reference solution. Such diagnostic measures are particularly useful for assessing the numerical reliability of PINNs applied to stiff and nonlinear differential systems (46–49).

The Mean Squared Error (MSE) is defined as Equation 23:

$$MSE_{PDE} = \frac{1}{N}\sum_{i=1}^{N}\left[R_f(\eta_i)^2 + R_\theta(\eta_i)^2 + R_\varnothing(\eta_i)^2\right] \tag{23}$$

where R_f, $R_\theta, R_\varnothing$ represents the governing-equation residual evaluated at the ith collocation point. A smaller MSE means that the model is able to match the overall shape and size of the solution across the whole domain.

The Root Mean Squared Error (RMSE) is calculated as

$$RMSE_{PDE} = \sqrt{\frac{1}{N}\sum_{i=1}^{N}\left[R_f(\eta_i)^2 + R_\theta(\eta_i)^2 + R_\varnothing(\eta_i)^2\right]} \tag{24}$$

The RMSE provides a quantitative measure of the overall magnitude of the residual errors and gives greater emphasis to comparatively larger deviations because the errors are squared before averaging. A lower RMSE indicates that the trained PINN satisfies the governing physical equations with smaller residual errors across the computational domain. Therefore, RMSE serves as a useful numerical indicator for assessing the convergence and consistency of the proposed physics-informed solution.

The Mean Absolute Error (MAE) is defined as Equations 25-27:

$$MAE_f = \frac{1}{N}\sum_{i=1}^{N}\left|R_f(\eta_i)\right| \tag{25}$$

$$MAE_\theta = \frac{1}{N}\sum_{i=1}^{N}\left|R_\theta(\eta_i)\right| \tag{26}$$

$$MAE_\varnothing = \frac{1}{N}\sum_{i=1}^{N}\left|R_\varnothing(\eta_i)\right| \tag{27}$$

Unlike MSE and RMSE, MAE is based on the absolute magnitude of the residual errors and is consequently less sensitive to isolated large errors. The simultaneous use of MSE, RMSE, and MAE provides complementary information regarding the magnitude and distribution of the residual errors in the trained PINN. In the present study, these metrics are employed as supplementary numerical diagnostics together with the governing-equation residuals, boundary-condition errors, and engineering quantities. The MSE, RMSE, and MAE are calculated from the governing-equation residuals evaluated at the collocation points. These quantities measure the magnitude of the residuals and indicate how closely the predicted functions satisfy the differential equations at those points. Lower residual values indicate better satisfaction of the imposed equations, but they do not directly quantify the difference between the predicted profiles and an independently computed solution. Therefore, these metrics are interpreted as residual-based convergence diagnostics rather than as direct measures of predictive error. Solution accuracy is assessed separately through comparison with the independent boundary-value solution, as described in Section 3.11 Thus, the reliability of the proposed framework is assessed from both a physics-based perspective and a quantitative convergence perspective. Recent advances in PINN-based modelling emphasize the importance of quantitative error measures for evaluating the numerical performance of neural-network solutions to nonlinear differential systems (41, 47–49). Accordingly, the combined assessment using MSE, RMSE, MAE, engineering quantities, boundary-condition errors, and governing-equation residuals provides a comprehensive evaluation of the proposed PINN methodology

for solving the nonlinear coupled Casson nanofluid boundary-layer problem with thermal stratification and multiphysical transport effects.

3.11 Independent numerical validation

To independently assess the accuracy of the proposed physics-informed neural network, the transformed governing Equations 7–9, together with the boundary conditions given in Equation 10, are solved using a conventional numerical boundary-value method. The numerical solution is obtained independently of the PINN training procedure using a high-accuracy boundary-value solver. The same dimensionless parameters, computational domain, governing equations, and boundary conditions are used in both approaches to ensure a consistent comparison.

The independent numerical solution is used as a reference for evaluating the velocity, temperature, and concentration profiles, denoted by $f(\eta), \theta(\eta)$, and $\phi(\eta)$, respectively. The comparison is performed for several representative parameter combinations, including a baseline case and cases corresponding to different levels of momentum, thermal, and concentration transport effects. The numerical solver employs a refined computational discretization and stringent convergence tolerances. The stability of the reference solution is checked by refining the numerical mesh and tightening the solver tolerances.

The accuracy of the PINN is evaluated by comparing its predictions with the corresponding reference solutions at common values of the similarity variable. In addition to the complete solution profiles, the wall quantities $f''(0)$, $-\theta'(0)$, and $-\phi'(0)$ are compared to assess the accuracy of the predicted wall shear, heat-transfer, and mass-transfer characteristics. The pointwise absolute error and the relative error in the wall quantities are calculated to quantify the differences between the two approaches.

It is emphasized that the MSE, MAE, and RMSE reported in Section 3.10 measure the governing-equation residuals and are used as internal convergence diagnostics. The additional comparison with the independently computed numerical solution provides a separate assessment of the agreement between the PINN predictions and a conventional numerical reference.

4 Results and discussion

The numerical results obtained using the proposed physics-informed neural network (PINN) are presented and discussed to assess the coupled flow, heat-transfer, and mass-transfer behaviour of the conducting Casson nanofluid. Particular attention is given to the effects of magnetic and porous-medium resistance on the momentum field, Casson rheology on flow and thermal transport, and the combined influence of Brownian motion and thermophoresis on the temperature and concentration distributions. The effects of thermal stratification, Schmidt number, and other relevant thermal and concentration-transport parameters are also examined. The predictive capability of the PINN is quantitatively assessed using the skin-friction coefficient, local Nusselt number, local Sherwood number, and statistical error measures, including MSE, MAE, and RMSE. These analyses are performed to address the objectives of the study and to establish the ability of the PINN to capture the strongly coupled nonlinear transport behaviour of the conducting Casson nanofluid.

4.1 Validation through engineering quantities

A first assessment of the proposed PINN is performed through the engineering quantities of interest, namely the skin-friction coefficient, local Nusselt number, and local Sherwood number. These quantities are particularly important because they provide an integrated measure of the wall shear stress, heat-transfer rate, and mass-transfer rate, respectively. The results obtained for different combinations of the governing parameters are summarized in Tables 5–7.

4.1.1 Skin-friction coefficient

Table 2 presents the predicted local skin-friction coefficient for different values of the Casson parameter, magnetic parameter, and porous-medium parameter. For the first set of calculations, with the magnetic parameter and porous-medium parameter fixed at 0.3 and 0.4, respectively, the skin-friction coefficient increases from 1.00704 to 1.35109 as the Casson parameter increases from 0.5 to 1.5. A similar increase is observed for the second parameter combination, for which the skin-friction coefficient increases from 1.03953 to 1.39467. These results demonstrate that the non-Newtonian rheological parameter has a pronounced influence on the wall shear response. The increase in the skin-friction coefficient indicates an enhancement in the wall shear associated with the modified rheological behaviour of the Casson fluid. Since the Casson parameter controls the relative contribution of yield-stress effects to the momentum transport, its variation changes the velocity gradient at the wall. The corresponding increase in the wall-gradient magnitude is reflected directly in the skin-friction coefficient. The effect of the porous-medium parameter is also evident in Table 5. For fixed values of the other parameters, increasing the porous-medium parameter from 1.0 to 2.0 increases the skin-friction coefficient from 1.00073 to 1.10994. This behaviour is consistent with the presence of Darcy resistance in the momentum equation. Increased porous resistance opposes the fluid motion and consequently increases the velocity gradient required to satisfy the wall condition. Therefore, the wall shear stress increases. Overall, the values reported in Table 5 range from approximately 1.0007 to 1.3947. The systematic variation of the skin-friction coefficient with the governing parameters confirms that the PINN is able to capture the sensitivity of the wall momentum transfer to non-Newtonian rheology, magnetic interaction, and porous-medium resistance. The results directly address the first and second objectives of the study concerning the influence of Casson behaviour and magnetic/porous effects on momentum transport.

4.1.2 Local Nusselt number

The predicted local Nusselt numbers are summarized in Table 6. The results demonstrate that the heat-transfer rate is strongly dependent on the coupled thermal and transport parameters. For example, increasing the first parameter in the first group from 0.5 to 1.5 reduces the Nusselt number from 0.601418 to 0.522155. Similarly, increasing the second parameter from 0.4 to 2.0 produces a decrease in the Nusselt number from 0.601418 to 0.469221. A particularly clear trend

TABLE 5 Skin-friction coefficient for different values of the governing parameter.

β	K_p	M	$-f'(0)$
0.5	0.3	0.4	1.00703991
1			1.23336695
1.5			1.35108581
0.5	0.5		1.03952501
1			1.27315291
1.5			1.39466914
0.3	1	1	1.00073443
		1.5	1.05674182
		2	1.10993925

TABLE 6 Local Nusselt number for different values of the governing parameters.

β	M	R_d	Pr	T	Q	Ec	$-\theta'(0)$
0.5	0.4	0.3	1.1	0.1	0.1	0.1	0.601418
1							0.549145
1.5							0.522155
0.5							0.601418
	1						0.548098
	1.5						0.507282
	2						0.469221
	0.4						0.601418
		0.5					0.539102
		1					0.437735
		1.5					0.377488
		0.3	1				0.566526
			1.2				0.634981
			1.4				0.698304
			1.6				0.756930
			1.1				0.601418
				0.2			0.581779
				0.4			0.541603
				0.6			0.500223
				0.1			0.601418
					0.2		0.528925
					0.3		0.433316
					0.4		0.280874
					0.1		0.601418
						0.2	0.493772
						0.4	0.278318
						0.6	0.062649

is observed for the parameter associated with thermal radiation. As this parameter increases from 0.3 to 1.5, the local Nusselt number decreases from 0.601418 to 0.377488. This reduction indicates that the increasing radiative contribution modifies the effective thermal diffusion process and increases the thermal energy stored within the boundary layer. Consequently, the wall temperature gradient is reduced and the dimensionless heat-transfer coefficient decreases. In contrast, the heat-generation parameter produces an increasing trend in the local Nusselt number. When the corresponding parameter is increased from 1.0 to 1.6, the predicted Nusselt number increases from 0.566526 to 0.756930. This indicates that the additional energy introduced into the thermal field substantially modifies the temperature gradient near the surface. The Brownian-motion parameter produces a progressive reduction in the Nusselt number. For the corresponding sequence of parameter values, the Nusselt number decreases from 0.601418 to 0.500223. This behaviour reflects the strong coupling between nanoparticle motion and thermal transport. Brownian diffusion modifies the temperature field through the cross-diffusion terms appearing in the energy equation, thereby changing the wall thermal gradient. A similar reduction is obtained with increasing thermophoretic effects. The local Nusselt number decreases from 0.601418 to 0.062649 over the investigated parameter range. This is one of the most pronounced variations in Table 3 and indicates that thermophoretic transport has a strong influence on the thermal boundary layer. The redistribution of nanoparticles induced by the temperature gradient modifies the coupled thermal field and consequently reduces the wall heat-transfer gradient. Thus, the Nusselt-number results demonstrate that the proposed PINN successfully captures the coupled thermal response of the conducting Casson nanofluid. Across the investigated cases, the local Nusselt number varies from 0.062649 to 0.756930. These results directly support the objectives concerning dissipative heating, thermal radiation, Brownian motion, thermophoresis, thermal stratification, and heat generation.

TABLE 7 Local Sherwood number for different values of the governing parameters.

Sc	c	Nt	Nb	$-\phi'(0)$
0.2	0.1	0.2	0.3	0.04465
			0.4	0.11800
			0.6	0.19142
	0.3		0.5	0.19234
			0.7	0.24267
			0.9	0.27055
0.1		0.1	0.3	0.12789
			0.4	0.16687
			0.5	0.19025
0.2	0.5	0.2	0.7	0.27298
			0.9	0.30085
			1.1	0.31849

4.1.3 Local Sherwood number

The predicted local Sherwood numbers are given in Table 7. The results quantify the influence of the governing transport parameters on the nanoparticle/species mass-transfer rate. For the first parameter combination, increasing the fourth parameter from 0.3 to 0.6 increases the Sherwood number from 0.04465 to 0.19142. This substantial increase demonstrates that the mass-transfer rate is highly sensitive to the corresponding concentration-transport parameter. A similar increasing trend is observed in the second set of cases, where the Sherwood number increases from 0.19234 to 0.27055 as the

TABLE 8 Independent numerical validation of the PINN solution for representative parameter combinations.

Parameter case	Quantity	PINN prediction	Independent BVP reference	Relative error (%)
Baseline	$f''(0)$	−0.918339	−0.918320	0.0020
Baseline	$\theta'(0)$	0.649831	0.650014	0.0282
Baseline	$\phi'(0)$	0.474062	0.473932	0.0275
Thermal variation R_d=1.5	$f''(0)$	−0.918350	−0.918320	0.0033
Thermal variation R_d=1.5	$\theta'(0)$	0.407675	0.407919	0.0598
Thermal variation R_d=1.5	$\phi'(0)$	0.635052	0.635162	0.0174
Concentration variation S_c=0.6	$f''(0)$	−0.918412	−0.918320	0.0100
Concentration variation S_c=0.6	$\theta'(0)$	0.656737	0.656863	0.0190
Concentration variation S_c=0.6	$\phi'(0)$	0.125781	0.126364	0.4617

corresponding parameter increases from 0.5 to 0.9. In the final group, the local Sherwood number increases from 0.27298 to 0.31849 as the investigated parameter changes from 0.7 to 1.1. These results demonstrate that the concentration boundary layer is strongly influenced by the parameters governing species diffusion, stratification, and nanoparticle migration. The overall Sherwood-number range is 0.04465–0.31849. The absence of negative values in Table 7 indicates that the predicted mass-transfer response remains positive for all investigated parameter combinations under the adopted sign convention. This is important because the local Sherwood number is directly associated with the wall concentration gradient, and its positive values indicate a consistent direction of mass transfer at the wall. The results in Table 7 therefore provide quantitative evidence that the PINN can resolve the concentration field and its wall gradient while maintaining physically consistent behaviour.

4.2 Independent validation of the PINN solution and collocation-point sensitivity analysis

To evaluate the numerical accuracy of the proposed physics-informed neural network (PINN), its predictions were compared with independently obtained numerical solutions of the governing boundary-value problem (BVP). The reference solutions were calculated using a conventional numerical BVP solver under the same governing equations, parameter values, and boundary conditions used for the PINN model. Three representative cases were considered: the baseline configuration, a thermal-radiation variation with $R_d = 1.5$, and a concentration-variation case with $S_c = 0.6$. The comparison was performed using the wall quantities $f''(0)$, $-\theta'(0)$, and $-\phi'(0)$, representing the skin-friction-related quantity, the dimensionless heat-transfer rate, and the dimensionless mass-transfer rate, respectively. Table 8 presents the PINN predictions, the corresponding BVP reference values, and the relative percentage errors for the three cases.

For the three validation cases, the relative errors in the raw wall gradients remain below 0.462%. This agreement supports the numerical consistency of the PINN predictions for the tested configurations, while the broader parameter range requires separate assessment. These findings demonstrate numerical consistency between the two solution approaches for the selected cases; however, they should not be interpreted as validation of the physical assumptions or governing-equation formulation itself. A further comparison was conducted using the velocity, temperature, and concentration profiles. Figures 4a–c show the PINN predictions alongside the corresponding BVP reference solutions for the baseline, thermal-radiation variation, and concentration-variation cases, respectively. The close correspondence between the plotted profiles provides additional evidence of agreement between the two numerical approaches over the computational domain. The wall-quantity comparisons in Table 8 and the profile comparisons in Figure 4 therefore provide complementary assessments of the numerical performance of the proposed PINN framework for the cases examined.

The PINN predictions were compared with an independently computed boundary-value problem (BVP) solution for three representative cases: the baseline configuration, a thermal-radiation variation with $R_d = 1.5$, and a concentration-variation case with $S_c = 0.6$. The comparison was performed using the raw wall gradients $f''(0)$, $\theta'(0)$, $\phi'(0)$ as reported in Table 8, the relative errors range from approximately 0.0020 to 0.4617%, with the largest difference occurring in the concentration gradient for $S_c = 0.6$. The small differences observed in these wall quantities indicate close numerical agreement between the PINN and the independent BVP solution for the three tested cases. These findings support the numerical consistency of the computed solutions under the specified training configuration; they do not, by themselves, establish the validity of the physical assumptions or guarantee accuracy for all parameter combinations.

The sensitivity of the PINN solution to collocation-point density was examined using 100, 200, 400, and 1,000 points under the same training configuration. Table 3 shows that the final total loss varies between approximately 5.47×10^{-6} and 7.58×10^{-6}. The variation in the total loss is not strictly monotonic, indicating that increasing the number of collocation points does not necessarily produce a lower

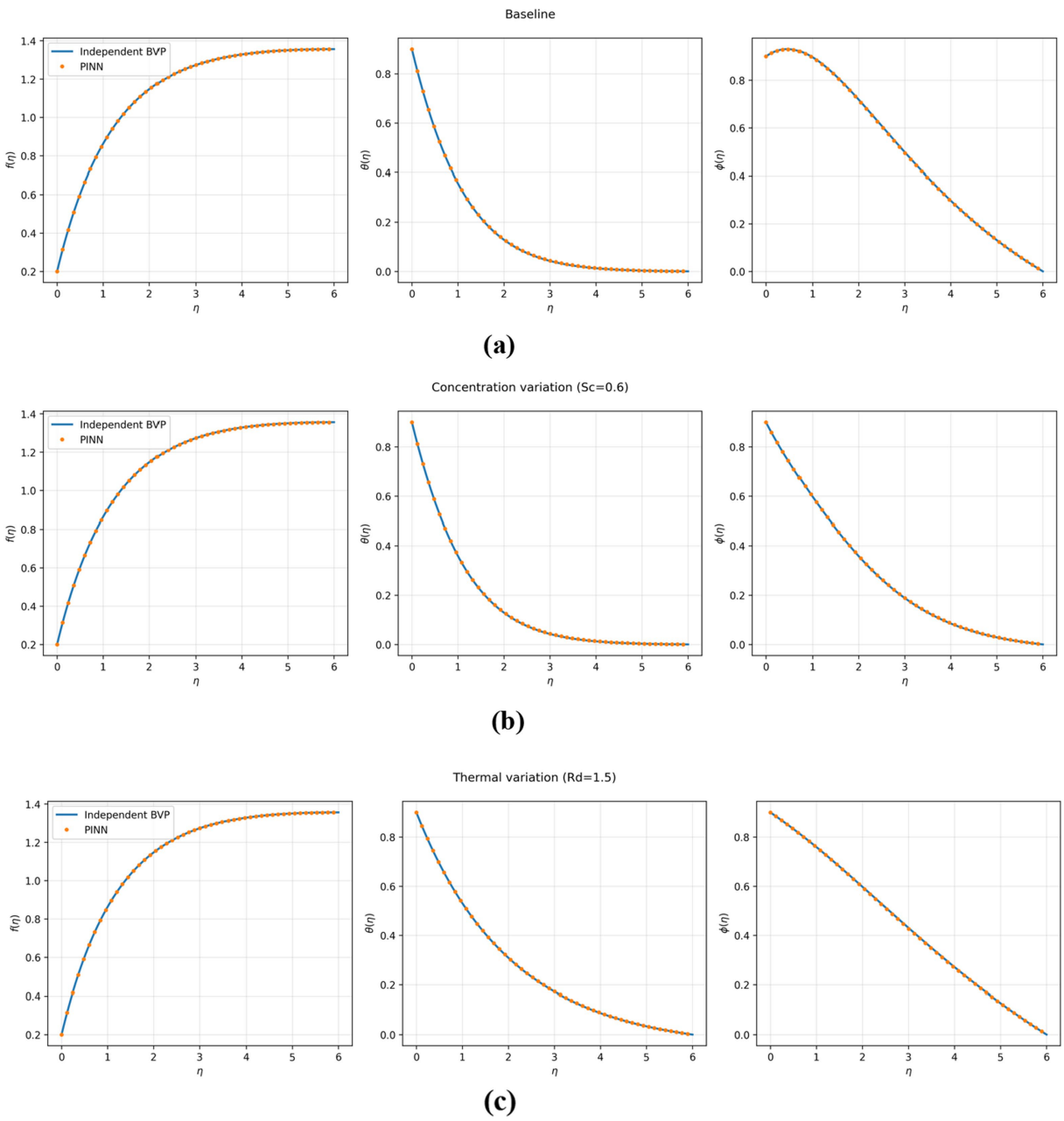


FIGURE 4
(a) Baseline case. **(b)** Thermal-radiation variation. **(c)** Concentration variation.

final loss under the selected optimization settings. The wall quantities show relatively small changes between successive point densities. The maximum relative changes are approximately 0.0231% for $f''(0)$, 0.1139% for $-\theta'(0)$, and 0.0430% for $\varnothing'(0)$. These values indicate that the wall-gradient predictions remain relatively stable over the tested point-density range for the baseline configuration. The profile comparisons provide a complementary assessment of the numerical solution. The MAE, RMSE, and maximum absolute error relative to the independent BVP solution remain small for the tested configurations. However, the profile errors do not decrease monotonically with increasing collocation-point density. This behaviour indicates that solution accuracy depends not only on the number of collocation points but also on the interaction between the training objective, optimization process, and coupled governing equations. Overall, the sensitivity analysis supports the numerical stability of the wall quantities for the baseline configuration over the tested range of 100 to 1,000 collocation points. This conclusion is restricted to the parameter configuration and training settings examined and should not be interpreted as proof of convergence for every parameter combination in the full model.

4.3 Residual-based convergence analysis

Table 9 presents the residual-based convergence diagnostics of the PINN for the investigated parameter combinations. The reported MSE ranges from 4.74×10^{-7} to 5.5486×10^{-3}, the MAE from approximately 4.7512×10^{-4} to 5.3159×10^{-2}, and the RMSE from 6.888×10^{-4} to 7.4489×10^{-2}. These quantities are calculated from the governing-equation residuals and characterize the extent to which the trained network satisfies the differential equations at the evaluation points.

TABLE 9 Physics-residual error and convergence metrics of the proposed PINN for different parameter combinations.

Measured Profiles	M	β	K_p	R_d	Pr	Ec	Nb	Nt	St	Q	Sc	Cr	Loss	MSE	MAE	RMSE
f'	0.1	0.5	0.3	0.3	1.1	0.1	0.1	0.1	0.1	0.1	0.2	0.1	8.89E-06	2.37E-06	0.00101825	0.0015403
f'	1.1												4.16E-05	8.03E-06	0.00185001	0.0028334
f'	2.1												3.37E-05	6.92E-06	0.00187359	0.0026305
f'	3.1												5.71E-06	1.54E-06	0.00078737	0.0012397
f'	0.1	0.1											3.64E-05	1.20E-05	0.00245706	0.0034661
f'		0.7											3.75E-06	1.04E-06	0.00069279	0.0010187
f'		1.4											3.22E-05	7.16E-06	0.00198029	0.0026756
f'		2.1											3.66E-05	1.04E-05	0.00156159	0.0032275
f'		0.5	0.1										4.36E-06	1.18E-06	0.00077095	0.0010881
f'			0.5										2.31E-06	7.45E-07	0.00051205	0.0008633
f'			1										6.76E-06	1.43E-06	0.000785	0.0011967
f'			1.5										0.000104	2.08E-05	0.00326211	0.0045636
θ		0.15	0.3										6.45E-05	1.65E-05	0.00245048	0.0040566
θ		0.21											0.000744	0.00024	0.00754021	0.0154919
θ		0.4											5.05E-06	9.06E-07	0.00064099	0.0009519
θ		1.75											1.17E-05	3.29E-06	0.00120193	0.0018125
θ		0.5											5.58E-06	1.49E-06	0.00071748	0.0012199
θ	1.1												5.47E-06	1.69E-06	0.00100798	0.0012992
θ	2.1												8.71E-06	2.28E-06	0.00097029	0.0015088
θ	3.1												0.000104	2.14E-05	0.00323206	0.0046274
θ													8.86E-05	1.91E-05	0.00285784	0.0043747
θ				0.7									7.39E-06	2.13E-06	0.00089631	0.0014602
θ				1.2									5.04E-06	1.66E-06	0.00084317	0.0012866
θ				2									2.93E-05	7.33E-06	0.00187617	0.002707
θ				0.3	1.5								0.00048	0.0001477	0.00660564	0.0121539
θ					2.2								0.00079	0.0002462	0.00722541	0.0156895
θ					2.9								3.54E-05	3.43E-06	0.00134511	0.0018511
θ					3.6								7.23E-05	1.13E-05	0.00246768	0.0033553
θ					1.1	0.2							2.88E-06	7.31E-07	0.00058813	0.0008548
θ						0.6							0.000163	1.15E-05	0.00243105	0.0033927
θ						1							3.18E-05	7.76E-06	0.00179916	0.0027857
θ						1.4							0.001643	0.0004028	0.0103162	0.0200702

(Continued)

TABLE 9 (Continued)

Measured Profiles	M	β	K_p	R_d	Pr	Ec	Nb	Nt	St	Q	Sc	Cr	Loss	MSE	MAE	RMSE
θ						0.1							3.27E-05	7.03E-06	0.00151405	0.0026507
θ							1.4						6.60E-05	2.09E-05	0.00222128	0.0045689
θ							2.4						4.66E-06	1.19E-06	0.00068193	0.0010902
θ							4.1						4.83E-06	1.60E-06	0.00092217	0.0012642
θ							0.1						0.000475	3.55E-05	0.0038623	0.0059591
θ								1.1					0.013047	0.0041048	0.04121672	0.0640686
θ								2.1					0.014532	0.0045848	0.04592196	0.0677108
θ								3.1					0.017655	0.0055486	0.053159	0.0744889
θ								0.1					0.000278	2.74E-05	0.00349227	0.0052361
θ									0.2				2.80E-06	8.83E-07	0.00061689	0.0009396
θ									0.3				0.000106	2.60E-05	0.00322188	0.0050988
θ									0.4				1.17E-05	1.80E-06	0.00095495	0.0013423
θ									0.1	0.2			4.85E-05	1.07E-05	0.00251587	0.0032683
θ										0.4			5.31E-05	6.39E-06	0.00162043	0.0025271
θ										0.6			5.28E-06	1.73E-06	0.00093494	0.0013138
θ										0.8			8.95E-05	1.78E-05	0.00301518	0.0042184
ϕ										0.1	0.1		0.0004	9.12E-05	0.00602628	0.0095475
ϕ											0.2		3.29E-05	7.77E-06	0.00183167	0.0027873
ϕ											0.3		2.59E-06	5.31E-07	0.00047512	0.0007284
ϕ											0.4		3.29E-06	1.09E-06	0.00070573	0.0010445
ϕ							0.2				0.2		2.72E-06	7.78E-07	0.00057683	0.000882
ϕ							0.3						0.000115	8.38E-06	0.00188034	0.0028953
ϕ							0.5						1.71E-06	5.46E-07	0.0004858	0.0007391
ϕ							1.7						1.51E-06	4.74E-07	0.00049117	0.0006888

The residual magnitudes vary across the parameter combinations, indicating that the numerical difficulty of satisfying the governing equations depends on the selected transport parameters and their nonlinear coupling. In particular, larger residual values occur for some parameter combinations, showing that residual satisfaction is not uniform throughout the investigated cases. These metrics are therefore used to characterize the residual convergence of the PINN, not to estimate its error relative to an independent solution.

The accuracy of the predicted solution is examined separately in Section 4.4 through comparisons with the independently computed boundary-value solution. This comparison provides evidence of agreement for the selected parameter cases, whereas the residual statistics in Table 5 characterize satisfaction of the governing equations. The two assessments are complementary and should not be interpreted as interchangeable measures of numerical accuracy.

4.4 Quantitative accuracy and PINN performance

Table 9 presents the quantitative convergence behaviour of the proposed PINN in terms of the total loss, Mean Squared Error (MSE), Mean Absolute Error (MAE), and Root Mean Squared Error (RMSE) for different combinations of the governing parameters. Unlike the engineering quantities, which describe the physical response of the system, these metrics quantify the magnitude of the residual errors associated with the trained neural-network solution. The results demonstrate that the proposed PINN achieves small residual errors for

most of the investigated parameter combinations. The minimum MSE obtained is 4.74×10^{-7}, whereas the maximum is 5.5486×10^{-3}. The MAE varies from approximately 4.7512×10^{-4} to 5.3159×10^{-2}, while the RMSE ranges from 6.888×10^{-4} to 7.4489×10^{-2}.

The relatively small residual values indicate that the neural-network solution satisfies the governing differential equations with a low residual magnitude at the evaluated collocation points. The lowest MSE values, particularly those below 10^{-6}. For example, an MSE of 4.74×10^{-7} is obtained together with an MAE of 4.7512×10^{-4} and an RMSE of 6.888×10^{-4}. The table also reveals that the error magnitude is not uniform across the complete parameter space. Relatively larger errors are observed for certain parameter combinations, particularly when the thermal or concentration transport parameters are increased substantially. For example, an MSE of 5.5486×10^{-3}, MAE of 5.3159×10^{-2}, and RMSE of 7.4489×10^{-2} are obtained for one of the more demanding parameter combinations. Such small residual errors indicate that the proposed network achieves a satisfactory level of numerical convergence for the corresponding parameter combinations. The variation in error magnitude across the parameter combinations indicates that the convergence behaviour of the PINN depends on the nonlinear coupling and parameter sensitivity of the governing system. Larger residuals for certain parameter combinations may be associated with stronger nonlinear interactions among the momentum, thermal, and concentration fields. Therefore, MSE, MAE, and RMSE provide useful quantitative diagnostics for evaluating the numerical convergence and stability of the proposed physics-informed framework. The reliability of the PINN is therefore assessed through the combined consideration of governing-equation residuals, boundary-condition errors, total loss, engineering quantities, and the physical consistency of the predicted velocity, temperature, and concentration profiles.

4.5 Influence of magnetic and porous-medium parameters on velocity

Figure 5 illustrates the effect of the magnetic parameter M on the dimensionless velocity profile. The magnetic parameter is varied over the range $0.1 \leq \mathrm{M} \leq 3.1$. A progressive reduction in the velocity profile is observed as M increases. The physical origin of this behaviour is the Lorentz force generated by the interaction between the electrically conducting fluid and the applied magnetic field. This force acts opposite to the fluid motion and therefore introduces additional resistance into the momentum boundary layer. As M increases, the velocity decreases more rapidly with the similarity variable, indicating a reduction in the momentum boundary-layer thickness. The strongest attenuation occurs for the larger magnetic parameter values, whereas the velocity remains comparatively higher for smaller M. This trend confirms that magnetic control provides an effective mechanism for suppressing the fluid motion. An important numerical observation is that all velocity profiles remain smooth and approach the far-field condition without oscillations. This behaviour indicates that the PINN successfully satisfies the asymptotic boundary condition while resolving the magnetic resistance over the complete computational domain. The result is directly relevant to the second objective of the study concerning the effect of electromagnetic resistance on momentum transport.

Figure 6 presents the influence of the porous-medium parameter K_p on the velocity distribution. Increasing K_p produces a progressive attenuation of the velocity profile. The porous medium introduces Darcy resistance into the momentum equation, thereby opposing fluid motion. As the resistance associated with the porous structure becomes stronger, the velocity decreases and the momentum boundary layer becomes thinner. The monotonic reduction of velocity with increasing porous-medium resistance is physically consistent with Darcy-type momentum transport. The result also complements the skin-friction behaviour reported in Table 5, where increasing porous resistance produces an increase in the wall shear response. Therefore, the combined graphical and tabular evidence demonstrates that porous-medium resistance significantly controls both the velocity field and the wall momentum transfer.

4.6 Effect of Casson rheology on velocity and temperature

Figure 7 shows the influence of the Casson parameter β on the velocity profile. The Casson parameter controls the degree of non-Newtonian behaviour through the yield-stress contribution. The numerical profiles demonstrate a systematic change in the velocity

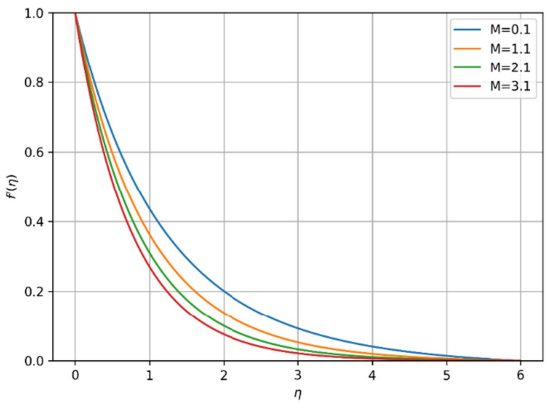


FIGURE 5
Effect of the magnetic parameter M on the dimensionless velocity profile. The remaining parameters are fixed at $\beta = 0.5$, $K_p = 0.4$, $Pr = 1.1$, $R_d = 0.3$, $Ec = 0.1$, $Nb = 0.1$, $N_t = 0.1$, $S_t = 0.1$, $Q = 0.1$, $Sc = 0.2$, $c = 0.1$, $Cr = 0.2$, and $S = 0.2$.

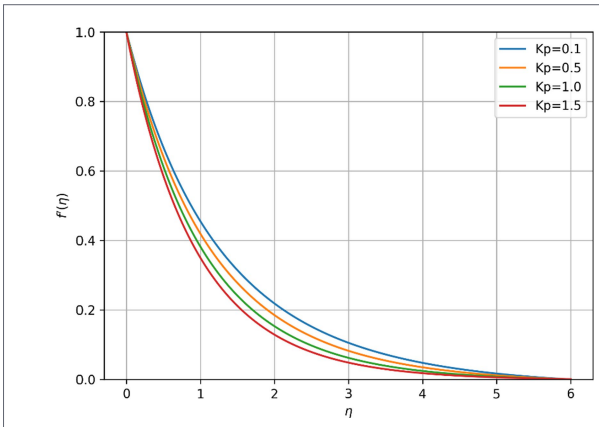


FIGURE 6
Effect of the porous-medium parameter K_p on the dimensionless velocity profile. The remaining parameters are fixed at $\beta = 0.5$, $M = 0.3$, $Pr = 1.1$, $R_d = 0.3$, $E_c = 0.1$, $N_b = 0.1$, $N_t = 0.1$, $S_t = 0.1$, $Q = 0.1$, $Sc = 0.2$, $c = 0.1$, $Cr = 0.2$, and $S = 0.2$.

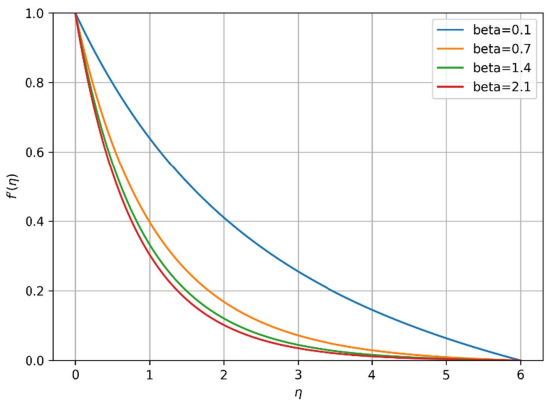


FIGURE 7
Effect of the Casson parameter β on the dimensionless velocity profile. The remaining parameters are fixed at M = 0.3, K_p = 0.4, Pr = 1.1, R_d = 0.3, Ec = 0.1, Nb = 0.1, N_t = 0.1, S_t = 0.1, Q = 0.1, Sc = 0.2, c = 0.1, Cr = 0.2, and S = 0.2.

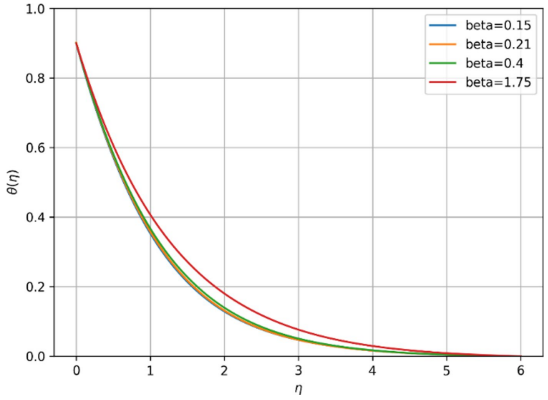


FIGURE 8
Effect of the Casson parameter β on the dimensionless temperature profile. The remaining parameters are fixed at M = 0.3, K_p = 0.4, Pr = 1.1, R_d = 0.3, Ec = 0.1, Nb = 0.1, N_t = 0.1, S_t = 0.1, Q = 0.1, Sc = 0.2, c = 0.1, Cr = 0.2, and S = 0.2.

distribution as the Casson parameter varies. The alteration of the velocity gradient reflects the transition in the rheological response of the fluid. The observed attenuation of the velocity profile with increasing Casson parameter indicates that the yield-stress contribution plays an important role in momentum transport. The corresponding changes in wall shear are also reflected in Table 5, where the skin-friction coefficient increases with the Casson parameter. Therefore, Figure 7 and Table 5 provide mutually consistent evidence that Casson rheology strongly influences the momentum boundary layer. Figure 8 further demonstrates that the Casson parameter also modifies the temperature distribution. The increase in yield-stress effects enhances resistance to fluid motion and consequently alters the conversion and redistribution of mechanical energy within the boundary layer. The resulting accumulation of thermal energy increases the temperature profile. The temperature profiles remain smooth and physically bounded for all investigated Casson parameter values. This confirms that the proposed PINN is capable of resolving the simultaneous influence of non-Newtonian momentum transport and thermal energy transport. The combined observations from Figures 7, 8 demonstrate that Casson rheology affects not only the velocity field but also the thermal response through the strong coupling between the momentum and energy equations.

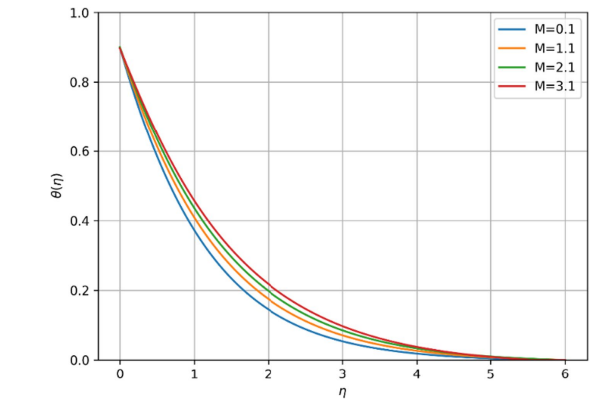


FIGURE 9
Effect of the magnetic parameter M on the dimensionless temperature profile. The remaining parameters are fixed at β = 0.5, K_p = 0.4, Pr = 1.1, R_d = 0.3, Ec = 0.1, Nb = 0.1, N_t = 0.1, S_t = 0.1, Q = 0.1, Sc = 0.2, c = 0.1, Cr = 0.2, and S = 0.2.

4.7 Magnetic effects on thermal transport

The effect of the magnetic parameter M on the temperature profile is shown in Figure 9. In contrast to its suppressing effect on velocity, increasing M enhances the temperature distribution. This apparent difference between the momentum and thermal responses arises from the dual role of the magnetic field in the present model. The magnetic field generates a Lorentz force that reduces the fluid velocity, but the associated electromagnetic interaction contributes to Joule heating in the energy equation. The additional heat generated within the fluid raises the temperature and increases the thermal boundary-layer thickness. Therefore, the magnetic parameter produces a simultaneous reduction in momentum transport and enhancement in thermal energy. This result is important for applications in which magnetic fields are used to regulate flow while simultaneously controlling thermal conditions. It also demonstrates the necessity of considering Joule heating when interpreting the thermal consequences of magnetic resistance. The result directly addresses the second objective of the study concerning the coupled effects of magnetic resistance and dissipative heating.

4.8 Thermal radiation and temperature distribution

Figure 10 presents the influence of the thermal radiation parameter R_d on the temperature profile. The parameter is investigated over approximately $0.3 \leq R_d \leq 2.0$. A clear increase in the temperature distribution is observed with increasing thermal radiation. The physical explanation lies in the additional radiative contribution to the energy transport. The Rosseland radiation approximation modifies the effective thermal diffusion process, allowing radiative energy transport to contribute to the thermal field. As R_d increases, the thermal energy available within the boundary layer increases, resulting in higher temperature values and a thicker thermal boundary layer. The graphical trend is consistent with the engineering results in Table 6, where changes in the radiation-related parameter produce a systematic variation in the local Nusselt number. Thus, thermal radiation acts

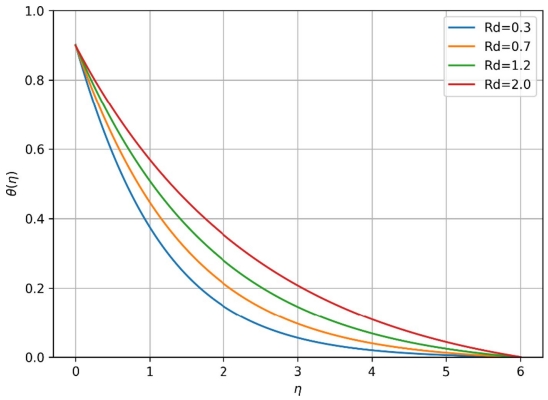


FIGURE 10
Effect of the thermal-radiation parameter R^d on the dimensionless temperature profile. The remaining parameters are fixed at $\beta = 0.5$, $M = 0.3$, $K_p = 0.4$, $Pr = 1.1$, $Ec = 0.1$, $Nb = 0.1$, $N_t = 0.1$, $S_t = 0.1$, $Q = 0.1$, $Sc = 0.2$, $c = 0.1$, $Cr = 0.2$, and $S = 0.2$.

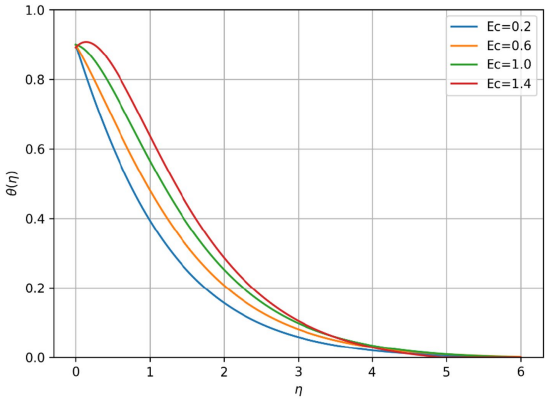


FIGURE 11
Effect of the Eckert number Ec on the dimensionless temperature profile. The remaining parameters are fixed at $\beta = 0.5$, $M = 0.3$, $K_p = 0.4$, $Pr = 1.1$, $R^d = 0.3$, $Nb = 0.1$, $N_t = 0.1$, $S_t = 0.1$, $Q = 0.1$, $Sc = 0.2$, $c = 0.1$, $Cr = 0.2$, and $S = 0.2$.

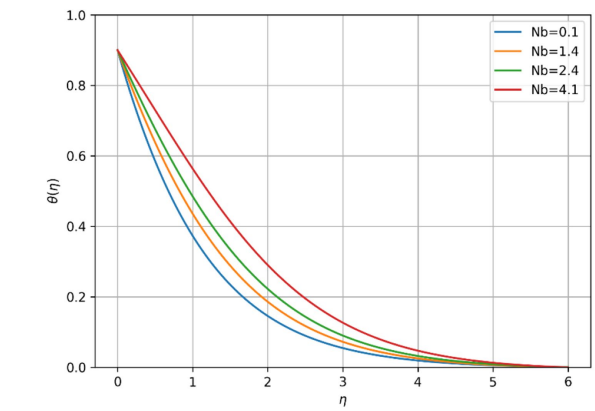


FIGURE 12
Effect of the Brownian-motion parameter $N\beta$ on the dimensionless temperature profile. The remaining parameters are fixed at $\beta = 0.5$, $M = 0.3$, $K_p = 0.4$, $Pr = 1.1$, $R_d = 0.3$, $Ec = 0.1$, $N_t = 0.1$, $S_t = 0.1$, $Q = 0.1$, $Sc = 0.2$, $c = 0.1$, $Cr = 0.2$, and $S = 0.2$.

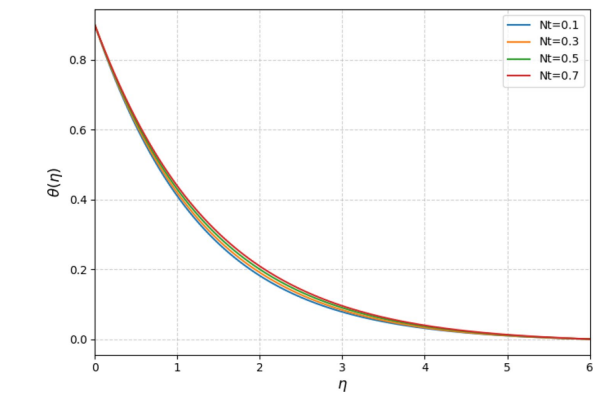


FIGURE 13
Effect of the thermophoresis parameter N_t on the dimensionless temperature profile. The remaining parameters are fixed at $\beta = 0.5$, $M = 0.3$, $K_p = 0.4$, $Pr = 1.1$, $R_d = 0.3$, $Ec = 0.1$, $N_b = 0.1$, $S_t = 0.1$, $Q = 0.1$, $Sc = 0.2$, $c = 0.1$, $Cr = 0.2$, and $S = 0.2$.

as an important control mechanism for the temperature field and wall heat-transfer characteristics.

4.9 Effect of Eckert number

The effect of the Eckert number Ec on the temperature field is depicted in Figure 11. The Eckert number represents the relative importance of viscous dissipation and therefore measures the conversion of kinetic energy into internal thermal energy. As Ec increases from approximately 0.2 to 1.4, the temperature profile increases systematically. The enhancement is associated with stronger viscous dissipation, which converts mechanical energy into thermal energy within the boundary layer. Consequently, the thermal field becomes hotter and the thermal boundary layer becomes thicker. The result demonstrates that dissipative heating cannot be neglected in strongly coupled MHD Casson nanofluid systems, particularly when the velocity gradients are significant. This observation is consistent with the modelling objective of incorporating both viscous and Joule dissipation into the energy transport equation.

4.10 Brownian motion and thermophoresis effects on temperature

Figures 12, 13 show the effects of the Brownian-motion parameter N_b and thermophoresis parameter N_t, respectively, on the temperature distribution. Increasing N_b enhances the temperature profile. Brownian motion represents the random movement of nanoparticles and increases the interaction between the dispersed nanoparticles and the surrounding fluid. Through the Brownian-motion contribution in the energy equation, this mechanism enhances thermal transport and modifies the temperature distribution. A similar enhancement is observed with increasing N_t. Thermophoresis drives nanoparticles from regions of higher temperature toward regions of lower temperature, thereby coupling the concentration and thermal fields. The resulting cross-diffusion modifies the energy distribution and increases the temperature profile. The simultaneous response of the temperature field to N_b and N_t demonstrates the importance of the Buongiorno-type nanoparticle transport mechanism used in the present model. Importantly, the profiles remain smooth for all investigated parameter values, confirming the numerical stability of the PINN

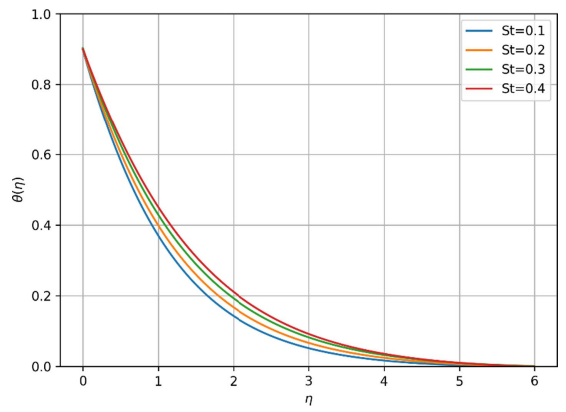


FIGURE 14
Effect of the thermal-stratification parameter S_t on the dimensionless temperature profile. The remaining parameters are fixed at $\beta = 0.5$, $M = 0.3$, $K_p = 0.4$, $Pr = 1.1$, $R^d = 0.3$, $Ec = 0.1$, $Nb = 0.1$, $N_t = 0.1$, $Q = 0.1$, $Sc = 0.2$, $c = 0.1$, $Cr = 0.2$, and $S = 0.2$.

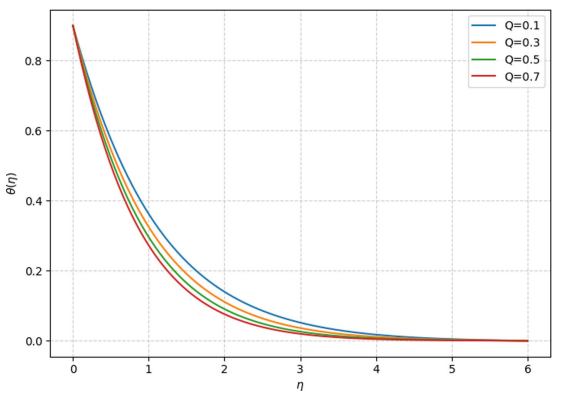


FIGURE 15
Effect of the heat-generation parameter Q on the dimensionless temperature profile. The remaining parameters are fixed at $\beta = 0.5$, $M = 0.3$, $K_p = 0.4$, $Pr = 1.1$, $R^d = 0.3$, $Ec = 0.1$, $Nb = 0.1$, $N_t = 0.1$, $S_t = 0.1$, $Sc = 0.2$, $c = 0.1$, $Cr = 0.2$, and $S = 0.2$.

solution. These observations directly address the third objective of the study concerning the coupled influence of Brownian motion and thermophoresis.

4.11 Thermal stratification and heat generation

Figure 14 presents the influence of the thermal stratification parameter S_t on the temperature distribution. Thermal stratification represents the spatial variation of the ambient temperature field. Increasing S_t reduces the effective temperature difference between the wall and the surrounding fluid and consequently modifies the thermal boundary layer. The numerical profiles show an increase in the temperature distribution with increasing thermal stratification parameter. The result demonstrates that the ambient thermal field has a substantial influence on the local temperature response and cannot be treated as spatially uniform when stratification is significant. This behaviour is relevant to thermal systems involving spatially varying environmental conditions, including solar thermal systems, atmospheric transport, and related heat-transfer configurations.

Figure 15 shows the effect of the heat-generation parameter Q. Increasing Q produces a clear enhancement in the temperature profile because the heat source directly introduces thermal energy into the fluid. The resulting temperature increase is accompanied by an increase in the thermal boundary-layer thickness. The combined results of Figures 14, 15 demonstrate that both environmental stratification and internal heat generation can significantly alter the thermal field. These results therefore provide direct support for the objective of analysing thermal stratification and energy-generation mechanisms in the conducting Casson nanofluid.

4.12 Schmidt number and Brownian motion effects on concentration

Figure 16 illustrates the influence of the Schmidt number S_c on the dimensionless concentration profile. The Schmidt number represents the ratio of momentum diffusivity to mass diffusivity and therefore plays an important role in controlling species or nanoparticle transport within the concentration boundary layer. The results show that increasing S_c reduces the concentration distribution and causes the concentration profile to approach its ambient value more rapidly.

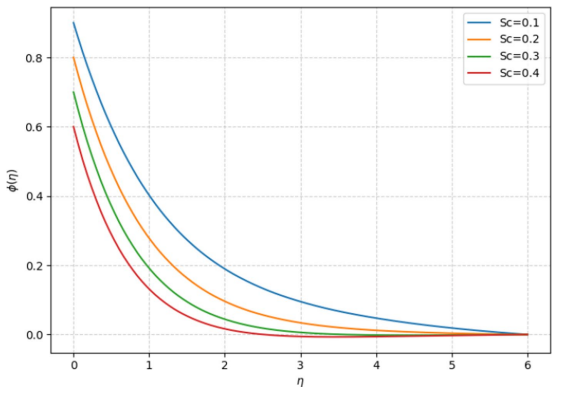


FIGURE 16
Effect of the Schmidt number Sc on the dimensionless concentration profile. The remaining parameters are fixed at $\beta = 0.5$, $M = 0.3$, $K_p = 0.4$, $Pr = 1.1$, $R_d = 0.3$, $Ec = 0.1$, $N_b = 0.1$, $N_t = 0.1$, $S_t = 0.1$, $Q = 0.1$, $c = 0.1$, $Cr = 0.2$, and $S = 0.2$.

This behaviour is associated with the reduction in mass diffusivity relative to momentum diffusivity as the Schmidt number increases. Consequently, the transport of nanoparticles or species through the concentration boundary layer becomes less diffusive, resulting in a thinner concentration boundary layer. The progressive reduction in concentration with increasing S_c demonstrates that mass-diffusion characteristics strongly influence the concentration field. The result is physically consistent with the role of the Schmidt number in the concentration equation and complements the mass-transfer predictions reported through the local Sherwood number. The smooth and monotonic profiles obtained for the investigated Schmidt-number values also demonstrate that the PINN captures the concentration response without introducing nonphysical oscillations.

Figure 17 illustrates the effect of the Brownian-motion parameter N_b on the concentration distribution. Increasing N_b reduces the concentration profile and decreases the concentration boundary-layer thickness. The enhanced random motion of nanoparticles promotes their redistribution within the fluid and consequently modifies the concentration gradient near the surface. This behaviour also demonstrates the coupled nature of the energy and concentration equations because Brownian motion simultaneously influences the temperature and concentration fields. The opposite responses of temperature and

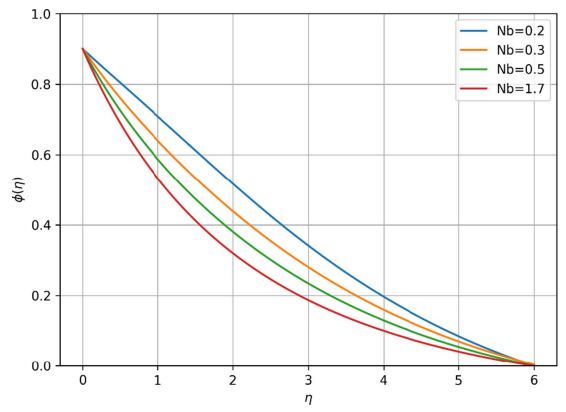


FIGURE 17
Effect of the Brownian-motion parameter $N\beta$ on the dimensionless concentration profile. The remaining parameters are fixed at $\beta = 0.5$, $M = 0.3$, $K_p = 0.4$, $Pr = 1.1$, $R_d = 0.3$, $Ec = 0.1$, $N_t = 0.1$, $S_t = 0.1$, $Q = 0.1$, $Sc = 0.2$, $c = 0.1$, $Cr = 0.2$, and $S = 0.2$.

concentration to Brownian motion are particularly significant. Figures 12, 17 show that increasing N_b enhances the temperature field while reducing the concentration field. This behaviour demonstrates the inherent cross-coupling between the energy and concentration equations. Such coupling is a central feature of the present nanofluid model and supports the third and fourth objectives of the study.

4.13 Overall physical interpretation and achievement of study objectives

The combined results from Tables 5–7 and Figures 5–17 demonstrate that the proposed PINN successfully captures the strongly coupled momentum, thermal, and concentration responses of the conducting Casson nanofluid.

First, the magnetic and porous-medium parameters provide effective mechanisms for controlling momentum transport. Increasing magnetic resistance suppresses the velocity through the Lorentz force, while porous-medium resistance produces a similar attenuation through Darcy drag. These effects are reflected in Figures 4, 5 and are quantitatively supported by the skin-friction results in Table 5. Second, Casson rheology substantially modifies the velocity and temperature fields. The yield-stress characteristics alter the wall shear response and influence the conversion and redistribution of energy within the boundary layer, as demonstrated by Figures 7, 8.

Third, the thermal response is strongly affected by radiation, magnetic/Joule heating, viscous dissipation, Brownian motion, thermophoresis, thermal stratification, and heat generation. Figures 9–15 collectively demonstrate that these mechanisms generally enhance the temperature field, although their influence on the wall heat-transfer rate can differ, as demonstrated by the Nusselt-number variations in Table 6. Fourth, Schmidt number and Brownian motion substantially modify the concentration field. The concentration profiles in Figures 16, 17 decrease with increasing values of the corresponding parameters, while the Sherwood-number results in Table 4 demonstrate that the wall mass-transfer response remains positive across the investigated parameter combinations. Finally, the statistical results in Table 7 provide quantitative evidence of the predictive capability of the PINN. The MSE reaches as low as 5.55×10^{-3}, while the corresponding MAE and RMSE remain below 5.32×10^{-2} and 7.45×10^{-2}, respectively, for the most accurate cases. Even for the more challenging parameter combinations, the model retains a finite and quantifiable error, demonstrating its ability to represent the nonlinear solution over a broad parameter space. The numerical performance of the PINN was evaluated using governing-equation residual metrics and independent comparison with a boundary-value solution. The independent validation covered the baseline parameter configuration, the increased thermal radiation case $R_d = 1.5$, and the increased Schmidt number case $S_c = 0.6$. For these cases, the comparison of the wall quantities showed agreement between the PINN and BVP solutions, with relative differences of approximately 0.0020 to 0.4617%across the reported quantities. These results support the numerical consistency of the PINN for the selected validation cases. However, residual-based diagnostics and validation for these cases alone do not establish solution accuracy or convergence for every parameter combination investigated.

Overall, the results establish that the proposed PINN provides a mesh-free predictive framework capable of simultaneously resolving the velocity, temperature, and concentration fields and the associated wall transport quantities. The combination of smooth converged profiles, physically consistent parameter trends, engineering-quantity predictions, and low statistical errors demonstrates that the proposed methodology is suitable for the nonlinear double-stratified conducting Casson nanofluid problem considered in this investigation.

5 Conclusion

The present study developed a physics-informed neural network (PINN) framework for predicting the coupled flow, heat-transfer, and mass-transfer characteristics of an electrically conducting Casson nanofluid over an exponentially expanding permeable surface. The formulated model incorporates Casson rheology, magnetic and porous-medium resistance, thermal radiation, viscous and Joule dissipation, Brownian motion, thermophoresis, thermal stratification, heat generation, Schmidt number, and chemical reaction. The nonlinear boundary-value problem was solved using a fully connected PINN with automatic differentiation and a two-stage Adam–L-BFGS optimization strategy. The results demonstrate that,

- Increasing the magnetic parameter M and porous-medium parameter K_p suppresses the velocity distribution because of the Lorentz and Darcy resistance forces, respectively, whereas variation of the Casson parameter β significantly modifies the non-Newtonian momentum and thermal fields.
- The thermal analysis shows that increasing the magnetic parameter, thermal radiation parameter R_d, Eckert number E_c, Brownian-motion parameter N_b, thermophoresis parameter N_t, thermal stratification parameter S_t, and heat-generation parameter Q enhances the temperature distribution.
- Enhanced Schmidt number S_c and Brownian-motion parameter N_b reduces the concentration profile and modifies the concentration boundary-layer thickness.
- The skin-friction coefficient varies from 1.0007 to 1.3947, the local Nusselt number ranges from 0.0626 to 0.7569, and the local Sherwood number varies from 0.0447 to 0.3185.
- A collocation-point sensitivity analysis was conducted using 100, 200, 400, and 1,000 points under the same training configuration. The wall quantities exhibited relatively small changes over the tested range, while the profile errors relative to the independent BVP solution remained small but did not decrease monotonically with increasing point density. These findings support the stability

of the predicted wall quantities for the baseline configuration; however, they do not establish universal convergence across all governing-parameter combinations. Further investigations may examine the sensitivity of the solution to collocation-point density across a wider range of parameter configurations and optimization settings.

- The residual-based convergence analysis gives MSE values ranging from 4.74×10^{-7} to 5.55×10^{-3}, MAE values from 4.75×10^{-4} to 5.32×10^{-2}, and RMSE values from 6.89×10^{-4} to 7.45×10^{-2}. These metrics quantify the residual satisfaction of the governing equations and are not interpreted as direct prediction errors. The agreement between the PINN and the independently computed boundary-value solution is assessed separately through comparisons of the solution profiles and wall quantities for the selected validation cases.
- The low governing-equation residuals and the comparison with an independently computed numerical reference provide evidence of the numerical performance of the PINN. The velocity, temperature, and concentration profiles are assessed alongside the residual errors and engineering quantities to evaluate the consistency of the computed solution.

Overall, the developed framework provides a mesh-free and computationally efficient approach for analysing multiphysical transport in conducting Casson nanofluids and offers a promising basis for future extensions to more complex geometries, parameter regimes, and coupled transport configurations.

Data availability statement

The computational code used in this study is publicly available at GitHub: https://github.com/cseprofamit/PINN-Conducting-Casson-Nanofluid-Flow. The repository provides the PINN implementation and associated computational materials for examining the governing equations and numerical results. The numerical results discussed in the manuscript are generated through the computational simulations described in the study. Any supplementary scripts or materials required to reproduce specific results are provided in the repository where applicable.

Author contributions

PM: Data curation, Formal analysis, Conceptualization, Investigation, Writing – original draft. AG: Formal analysis, Writing – review & editing, Methodology, Validation. SM: Investigation, Resources, Writing – review & editing. HS: Writing – review & editing.

Funding

The author(s) declared that financial support was not received for this work and/or its publication.

Conflict of interest

The author(s) declared that this work was conducted in the absence of any commercial or financial relationships that could be construed as a potential conflict of interest.

Generative AI statement

The author(s) declared that Generative AI was used in the creation of this manuscript. During the preparation of this manuscript, ChatGPT (OpenAI) was used solely to assist with manuscript writing, language improvement, grammar, clarity, readability, and presentation. ChatGPT was not used to generate or modify the research data, numerical results, research methodology, computational procedures, or scientific conclusions. All research design, mathematical modelling, computational analysis, results, interpretation, and conclusions were developed and verified by the authors. The authors reviewed and edited all AI-assisted content and take full responsibility for the accuracy, originality, and integrity of the final manuscript.

Any alternative text (alt text) provided alongside figures in this article has been generated by Frontiers with the support of artificial intelligence and reasonable efforts have been made to ensure accuracy, including review by the authors wherever possible. If you identify any issues, please contact us.

Publisher's note

All claims expressed in this article are solely those of the authors and do not necessarily represent those of their affiliated organizations, or those of the publisher, the editors and the reviewers. Any product that may be evaluated in this article, or claim that may be made by its manufacturer, is not guaranteed or endorsed by the publisher.

References

1. Sankari MS, Rao ME, Khan W, Alshehri MH, Eldin SM, Iqbal S. Analytical analysis of the double stratification on Casson nanofluid over an exponential stretching sheet. *Case Stud Therm Eng*. (2023) 50:103492. doi: 10.1016/j.csite.2023.103492

2. Kumar YS, Hussain S, Raghunath K, Ali F, Guedri K, Eldin SM, et al. Numerical analysis of magnetohydrodynamics Casson nanofluid flow with activation energy, hall current and thermal radiation. *Sci Rep*. (2023) 13:4021. doi: 10.1038/s41598-023-28379-5

3. Swain BK, Parida BC, Kar S, Senapati N. Viscous dissipation and joule heating effect on MHD flow and heat transfer past a stretching sheet embedded in a porous medium. *Heliyon*. (2020) 6:e05234. doi: 10.1016/j.heliyon.2020.e05234

4. Reddy BN, Maddileti P. Casson nanofluid and joule parameter effects on variable radiative flow of MHD stretching sheet. *Partial Differ Equ Appl Math*. (2023) 7:100487. doi: 10.1016/j.padiff.2023.100487

5. Alqarni MM, Bilal M, Allogmany R, Tag-Eldin E, Ghoneim ME, Yassen MF. Mathematical analysis of Casson fluid flow with energy and mass transfer under the influence of activation energy from a non-coaxially spinning disc. *Front Energy Res*. (2022) 10:1–10. doi: 10.3389/fenrg.2022.100123

6. Naseem T, Fatima U, Munir M, Shahzad A, Kausar N, Nisar KS, et al. Joule heating and viscous dissipation effects in hydromagnetized boundary layer flow with variable temperature. *Case Stud Therm Eng*. (2022) 35:102083. doi: 10.1016/j.csite.2022.102083

7. Khan Q, Farooq M, Ahmad S. Generalized transport analysis on mixed convection squeeze flow of a Casson fluid over an inclined stretching sheet with viscous dissipation and double stratification. *Ain Shams Eng J*. (2024) 15:102253. doi: 10.1016/j.asej.2023.102253

8. Khader MM, Babatin MM, Megahed AM. Numerical evaluation of Ohmic dissipation and thermal conductivity impacts on Casson fluid flow. *Case Stud Therm Eng*. (2023) 49:103192. doi: 10.1016/j.csite.2023.103192

9. Reddappa B, Parandhama A, Venkateswara Raju K, Sreenadh S. Boundary layer flow of thermally conducting Jeffrey fluid over a stratified exponentially stretching sheet. *Turk J Comput Math Educ*. (2021) 13:730–9.

10. Rehman KU, Shatanawi W, Malik MY. Heat transfer and double stratification phenomena in non-Newtonian liquid suspension: a comparative thermal analysis. *Case Stud Therm Eng*. (2022) 33:101934. doi: 10.1016/j.csite.2022.101934

11. Reza-E-Rabbi S, Arifuzzaman SM, Sarkar T, Khan MS, Ahmmed SF. Explicit finite difference analysis of unsteady MHD flow of a chemically reacting Casson fluid past a stretching sheet with Brownian motion and thermophoresis effects. *J King Saud Univ Sci*. (2020) 32:690–701. doi: 10.1016/j.jksus.2019.07.012

12. Liao S. *Beyond Perturbation: Introduction to the Homotopy Analysis Method*. New York: Chapman & Hall/CRC (2003).

13. Liao SJ. An optimal homotopy-analysis approach for strongly nonlinear differential equations. *Commun Nonlinear Sci Numer Simul*. (2010) 15:2003–16. doi: 10.1016/j.cnsns.2009.09.002

14. Anwar MS, Alqarni MS, Irfan M. Heat transfer in MHD convection at a stagnation point in non-Newtonian fluid with yield stress and chemical reactions. *Chin J Phys*. (2024) 89:1299–308. doi: 10.1016/j.cjph.2024.01.030

15. Ellahi R. Effects of MHD and temperature-dependent viscosity on non-Newtonian nanofluid flow in a pipe: analytical solutions. *Appl Math Model*. (2013) 37:1451–67. doi: 10.1016/j.apm.2012.04.004

16. Ashwinkumar GP, Samrat SP, Sandeep N. Convective heat transfer in MHD hybrid nanofluid flow over two different geometries. *Int Commun Heat Mass Transf*. (2021) 127:105563. doi: 10.1016/j.icheatmasstransfer.2021.105563

17. Ibrahim W, Negera M. Viscous dissipation effect on mixed convective heat transfer of MHD Williamson nanofluid over a stretching cylinder with variable thermal conductivity and chemical reaction. *Heat Transf*. (2021) 50:2427–53. doi: 10.1002/htj.21985

18. Yanala DR, Kumar MA, Bejawada SG, Nisar KS, Raju RS, Rao VS. Heat and mass transfer in 3-D radiative MHD Casson fluid flow over a stretching permeable sheet with chemical reaction. *Case Stud Therm Eng*. (2023) 51:103527. doi: 10.1016/j.csite.2023.103527

19. Narender G, Govardhan K, Sarma GS. MHD Casson nanofluid past a stretching sheet with viscous dissipation, chemical reaction and heat source/sink. *J Appl Comput Mech*. (2021) 7:2040–8. doi: 10.22055/JACM.2021.36877

20. Gopal D, Jagadha S, Sreehari P, Kishan N, Mahendar D. Numerical study of viscous dissipation with first-order chemical reaction and Ohmic effects on MHD nanofluid flow through an exponential stretching sheet. *Mater Today Proc*. (2022) 59:1028–33. doi: 10.1016/j.matpr.2022.05.123

21. Cuomo S, Di Cola VS, Giampaolo F, Rozza G, Raissi M, Piccialli F. Scientific machine learning through physics-informed neural networks: where we are and what's next. *J Sci Comput*. (2022) 92:88. doi: 10.1007/s10915-022-01939-z

22. Shukla K, Jagtap AD, Karniadakis GE. A review of physics-informed neural networks for solving PDEs. *Arch Comput Methods Eng*. (2023). doi: 10.1007/s11831-023-09935-0

23. Meng X, Li Z, Zhang D, Karniadakis GE. PPINN: parareal physics-informed neural network for time-dependent PDEs. *Comput Methods Appl Mech Eng*. (2020) 370:113250. doi: 10.1016/j.cma.2020.113250

24. Kim E, Kwon H, Cho S, Yeo K, Choi M. Stabilizing physics-informed neural networks for stiff differential equations: re-spacing layer. *Comput Math Appl*. (2025) 200:167–79. doi: 10.1016/j.camwa.2025.01.012

25. Karkadakattil A. A physics-stabilized self-updating digital twin framework using physics-informed neural networks for thermal field prediction. *Appl Comp Sys*. (2026) 31:30–40. doi: 10.2478/acss-2026-0004

26. Wang S, Teng Y, Perdikaris P. Understanding and mitigating gradient flow pathologies in physics-informed neural networks. *SIAM J Sci Comput*. (2021) 43:A3055–81. doi: 10.1137/20M1318043

27. Berman J, Peherstorfer B. CoLoRA: continuous low-rank adaptation for reduced implicit neural modeling of parameterized PDEs. *arXiv preprint*. (2024):arXiv:2402.14646

28. Galal AM, Haider Q, Arshad M, Hassan A, Alharbi FM, Alam MM, et al. Intelligent neural computing to investigate the heat and mass transmission in nanofluidic system between two rotating permeable disks: supervised learning mechanism. *Case Stud Therm Eng*. (2024) 59:104531. doi: 10.1016/j.csite.2024.104531

29. Hassan A, Haider Q, Alsubaie N, Alharbi FM, Alhushaybari A, Galal AM. Investigation of mixed convection in spinning nanofluid over rotating cone using artificial neural networks and BVP-4C technique. *Mathematics (Basel)*. (2022) 10:4833. doi: 10.3390/math10244833

30. Haider Q, Hassan A, Hajjej F, Alharbi FM, Saeed AM, Arshad M. Effect of thermal radiation on electrically conducting nanofluid with slip conditions and heat source using artificial neural networks. *BioNanoScience*. (2023) 13:2483–506. doi: 10.1007/s12668-023-01171-5

31. Haider Q, Hussain A, Rehman A, Ashour A, Althobaiti A. Mass and heat transport assessment and nanomaterial liquid flowing on a rotating cone: a numerical computing approach. *Nano*. (2022) 12:1700. doi: 10.3390/nano12101700

32. Haider Q, Sabir Z, Salahshour S, Ali MR, Tag Eldin ES, Sadat R. Magneto-hydraulic Casson fluid flow under the suction/blowing effects past over the porous stretching surface. *Waves Random Complex Media*. (2026) 35:14492–511. doi: 10.1080/17455030.2022.2149882

33. Chari FN, Ganji DD, Mahboobtosi M, Jalili P, Ganji AM, Jalili B. Heat transfer analysis of GO/water nanofluid flow under the influence of joule heating and chemical reactions with MHD: analytical and numerical concept. *Multiscale Multidiscip Model Exp Des*. (2025) 8:264. doi: 10.1007/s41939-025-00843-x

34. Ganji AM, Shateri A, Ehsani H, Mahboobtosi M, Domiri Ganji DD, Jalili B, et al. Data-driven prediction of thermo-solutal transport in sodium alginate-based Casson radiative magnetohydrodynamics ternary nanofluid squeeze flow. *Eng Sci Technol Int J*. (2026) 77:102363. doi: 10.1016/j.jestch.2026.102363

35. Jalili M, Ehsani H, Ganji AM, Shateri A, Mahboobtosi M, Wu Y, et al. Data- driven prediction of thermal and flow fields in magnetized Boger-micropolar tri-hybrid nanofluids via deep artificial neural networks. *Eng Appl Artif Intell*. (2025) 161:112232. doi: 10.1016/j.engappai.2025.11223

36. Ganji AM, Shateri A, Domiri Ganji DD, Jalili P, Jalili B. Physics-informed neural network coupled with semianalytical hybrid modeling of micropolar magnetohydrodynamic channel flow with heat and mass transport in a porous medium. *Phys Fluids*. (2025) 37:113115. doi: 10.1063/5.0301887

37. Ganji AM, Domiri Ganji DD, Jalili P, Jalili B. Physics-informed deep operator network for real-time dynamic simulation of extruded-absorber photovoltaic/thermal collectors. *Appl Therm Eng*. (2026) 289:129695. doi: 10.1016/j.applthermaleng.2026.129695

38. Galal AM, Haider Q, Alharbi FM, Alam MM. Application of Bayesian regularized neural networks for simulating blood nanofluid flow in stenotic arteries. *Int J Comput Math*. (2026) 103:27–40. doi: 10.1080/00207160.2025.2576540

39. Ganji AM, Shateri A, Jalili P, Jalili B, Domiri Ganji DD. Physics-informed deep operator learning framework for multiphysics heat and mass transport in rotating disk energy systems. *Results Eng*. (2026) 29:108283

40. Raissi M, Perdikaris P, Karniadakis GE. Physics-informed neural networks: a deep learning framework for solving forward and inverse problems involving nonlinear PDEs. *J Comput Phys*. (2019) 378:686–707. doi: 10.1016/j.jcp.2018.10.045

41. Karniadakis GE, Kevrekidis IG, Lu L, Perdikaris P, Wang S, Yang L. Physics-informed machine learning. *Nat Rev Phys*. (2021) 3:422–40. doi: 10.1038/s42254-021-00314-5

42. Faroughi SA, Pawar NM, Fernandes C, Raissi M, Das S, Kalantari NK, et al. Physics-guided, physics-informed, and physics-encoded neural networks and operators in scientific computing: fluid and solid mechanics. *J Comput Inf Sci Eng*. (2024) 24:040802. doi: 10.1115/1.4065187

43. De Ryck T, Mishra S. Numerical analysis of physics-informed neural networks and related models in physics-informed machine learning. *Acta Numer*. (2024) 33:633–713. doi: 10.1017/S096249292400003X

44. Jagtap AD, Karniadakis GE. Extended physics-informed neural networks (XPINNs): a generalized space-time domain decomposition deep learning framework for nonlinear PDEs. *Commun Comput Phys*. (2020) 28:2002–41. doi: 10.4208/cicp.OA-2020-0162

45. Liu S, Huang X, Protopapas P. "Residual-based error bound for physics-informed neural networks". In: *Proceedings of the 39th Conference on Uncertainty in Artificial Intelligence (UAI)*. Pittsburgh, PA: PMLR (2023). p. 1284–93.

46. De Ryck T, Jagtap AD, Mishra S. Error estimates for physics-informed neural networks approximating the Navier–stokes equations. *IMA J Numer Anal*. (2024) 44:83–119. doi: 10.1093/imanum/drad001

47. Shin Y, Zhang Z, Karniadakis GE. Error estimates of residual minimization using neural networks for linear PDEs. *J Mach Learn Model Comput*. (2023) 4:73–101. doi: 10.1615/JMachLearnModelComput.2023050411

48. Berrone S, Canuto C, Pintore M. Solving PDEs by variational physics-informed neural networks: an a posteriori error analysis. *Ann Univ Ferrara*. (2022) 68:575–95. doi: 10.1007/s11565-022-00391-7

49. Goraya S, Sobh N, Masud A. Error estimates and physics informed augmentation of neural networks for thermally coupled incompressible Navier stokes equations. *Comput Mech*. (2023) 72:267–89. doi: 10.1007/s00466-023-02288-5